

**NASA**  
**Technical**  
**Paper**  
**3221**

1992

# A Nozzle Internal Performance Prediction Method

John R. Carlson  
*Langley Research Center*  
*Hampton, Virginia*

**NASA**

National Aeronautics and  
Space Administration  
Office of Management  
Scientific and Technical  
Information Program

## Abstract

*A prediction method has been written and incorporated into a three-dimensional Navier-Stokes code (PAB3D) for the calculation of nozzle internal performance. The quantities calculated are discharge coefficient; normal, side, and axial thrust ratios; rolling, pitching, and yawing moments; and effective pitch and yaw vector angles. Four different case studies are presented to confirm the applicability of the methodology. Internal and, in most situations, external flow-field regions are required to be modeled. The computed nozzle discharge coefficient matches both the level and the trend of the experimental data within quoted experimental data accuracy (0.5 percent). Moment and force ratios are generally within 1 to 2 percent of the absolute level of experimental data, with the trends of the data matched accurately.*

## Introduction

Highly maneuverable aircraft operate over power settings and Mach numbers that require a propulsion system with variable geometry for obtaining efficient performance at different throttle settings. Understanding the effects of various nozzle geometries on internal flow and on the surrounding boattail-nozzle region is vital for designing efficient afterbodies for these aircraft. The development and utilization of advanced computational methods plays a vital role in developing this understanding. Presently, there are several ongoing research activities at the Langley Research Center directed at establishing an experimental data base for new nozzle concepts. Subsequent improvements to the computational methods are guided by these data.

A nozzle internal performance module has been written, and the prediction capabilities of this module have been evaluated for a series of test cases. The module was incorporated into the Navier-Stokes solver PAB3D (ref. 1), which provides the flow-field solution for the prediction subroutine. The control volume concept was used for the calculation of the resultant body forces due to the fluid flow exiting the nozzle (ref. 2). Forces and moments are calculated from the integration of the momentum fluxes through the volume faces. These integrations can be performed at intermediate steps throughout the solution procedure to provide a flow convergence quantity and to monitor the flow code's computational residuals.

This paper presents four nozzle case studies for evaluation of the performance prediction methodology. Each nozzle geometry has characteristics that require the calculation of different flows and performance quantities for each case. Comparisons of computed discharge coefficient, axial thrust ratio, resul-

tant vector angles, and pitching and yawing moments with experimental data are presented as appropriate for the following cases.

*Case 1:* The first case study is from the series of Stratford choke nozzles (ref. 3) that serves as the calibration standard for many propulsion testing facilities. These geometries are convergent nozzles with a circular-arc internal closure contour through the throat. These nozzles have well-established mass-flow characteristics that provide a highly accurate standard for comparisons of performance predictions. A grid convergence study of discharge coefficient is shown for the nozzle with a throat area of 25.766 cm<sup>2</sup> (3.992 in<sup>2</sup>) operating at a pressure ratio of 2.

*Case 2:* The capability of predicting discharge coefficient and axial forces for a type of convergent-divergent (C-D) nozzle is verified with the experimental data of Mason, Putnam, and Re (ref. 4). Their data were obtained on a model designed to address the performance characteristics due to parametric changes of nozzle internal geometry. The nozzle throat contour, that is, the radius of the circular-arc throat contour, was systematically changed in a series of nonaxisymmetric C-D nozzles with parallel sidewalls. Internal static pressures, thrust ratio, and discharge coefficient data for various nozzle operating pressure ratios were measured. Low- and high-expansion-ratio geometry nozzles were investigated. For this study, comparisons of prediction with experimentally determined nozzle discharge coefficient, thrust ratio, and centerline divergent flap static pressures are presented for the low-expansion-ratio nozzles only.

*Case 3:* The third geometry provided data to evaluate the prediction of side forces coupled with axial forces. The translating sidewall yaw vector concept tested by Mason and Berrier (ref. 5) was one

of several yaw vector concepts on which discharge coefficient, thrust ratio, resultant thrust ratio, and effective pitch and yaw vector angles were measured. Comparisons of prediction with an experimentally determined effective yaw vector angle are presented.

*Case 4:* The axisymmetric nozzle with multi-axis thrust vectoring that was tested experimentally by Carson and Capone (ref. 6) provided data for evaluation of the prediction of pitching moments coupled with yawing moments. Five combinations of geometric pitch and yaw vector angles were tested in dry power and afterburning power settings for two different lengths of divergent flaps. The nozzle expansion ratio was 1.35 for both settings, and thus the design nozzle pressure ratio was 5.01. A dry power setting would be a throat area permitting a particular mass flow indicative of aircraft cruise thrust levels. The data available include discharge coefficient and forces, moments, and internal static pressures at several angular stations around the nozzle. Only performance data from the short-flap, dry power nozzle are presented.

## Symbols and Abbreviations

$A$	nozzle cross-sectional area, $\text{cm}^2$	$M_\infty$	free-stream Mach number
$A_e$	nozzle exit area, $\text{cm}^2$	$N_{pt}$	number of grid points
$A_t$	nozzle throat area, $\text{cm}^2$	NPR	nozzle pressure ratio, $\frac{p_{t,j}}{p_\infty}$
$A^*$	nozzle cross-sectional area at sonic conditions, $\text{cm}^2$	NPR <sub>d</sub>	design nozzle pressure ratio
AR	nozzle aspect ratio, ratio of width to height at exit	$\mathbf{n}$	surface normal vector
$a$	local speed of sound, m/sec	$p$	static pressure, Pa
$C_d$	discharge coefficient, $\frac{w_p}{w_i}$	$p_t$	total pressure, Pa
$e$	energy, J	$p_{t,j}$	jet total pressure, Pa
$F$	gross thrust along body axis, N	$p_\infty$	free-stream static pressure, Pa
$\mathbf{F}$	total force vector, N	$R$	gas constant ( $\gamma = 1.4$ ), 287.3 J/kg-K
$F_i$	ideal isentropic gross thrust along body axis, N	$\mathbf{R}$	moment arm vector, cm
$l$	length from nozzle connect station to nozzle exit station, cm	$r_c$	nozzle circular-arc throat radius, cm
$l_s$	axial length from nozzle throat to nozzle exit, cm	$T$	static temperature, K
$\mathbf{M}$	total moment vector, N	$T_t$	total temperature, K
$M_d$	isentropic nozzle exit Mach number	$T_{t,j}$	jet total temperature, K
$M_i$	local jet Mach number	$\mathbf{U}$	total velocity vector, m/sec
		$u$	velocity in streamwise direction, m/sec
		$u_e$	velocity at edge of boundary layer, m/sec
		$w_i$	ideal mass-flow rate, kg/sec
		$w_p$	calculated mass-flow rate, kg/sec
		$x$	axial distance measured from nozzle throat, positive downstream, cm
		$x_s$	axial distance from nozzle connect station to end of left sidewall, cm
		$x_t$	axial distance from nozzle connect station to nozzle throat station, cm
		$y^+$	nondimensional distance from wall in a turbulent shear layer
		$z$	vertical ordinate, cm
		$\gamma$	ratio of specific heats, 1.4 for air
		$\Delta A$	incremental cross-sectional area, $\text{cm}^2$
		$\delta_{v,p}$	pitch vector angle, deg
		$\delta_{v,y}$	yaw vector angle, deg
		$\delta_y$	effective yaw vector angle, deg
		$\epsilon$	nozzle expansion ratio, $\frac{A_e}{A_t}$
		$\theta$	nozzle convergence flap angle, deg
		$\nu$	kinematic viscosity, $\text{m}^2/\text{sec}$
		$\rho$	density, $\text{kg}/\text{m}^3$

## Experimental Data

A sketch of a representative test model is presented in figure 1. The Stratford nozzle geometry is shown in figure 2. Discharge coefficient data for the Stratford nozzle were obtained from the static thrust tables in the data reduction system used by the Langley 16-Foot Transonic Tunnel. The other three nozzle geometries chosen for this evaluation were tested in the static test facility of the 16-Foot Tunnel. The two nozzles reported in references 4 and 5 were non-axisymmetric C-D type designs with circular-arc throat contours, straight divergent flaps, and flat nondiverging sidewalls; the relevant geometric parameters are shown in figures 3 and 4. The nozzle reported in reference 6 (case 4) was an axisymmetric C-D type with a sharp throat corner, as shown in figure 5 for the unvectored geometry. Figure 6 presents sketches of this nozzle at several thrust-vectoring angles. For each nozzle, the jet was simulated by high-pressure air exhausting out the exit of the nozzle into static air. The nozzle discharge coefficient was determined from the experimentally measured jet total temperature, jet total pressure, and mass-flow rate. Thrust ratio was determined from the measured balance axial force that was nondimensionalized by the ideal thrust (determined from the measured nozzle mass flow). Multiaxis force measurements were determined from a six-component force balance.

## Computational Procedure

### Flow-Field Calculation

A three-dimensional Navier-Stokes code PAB3D has been under development with specific applications for predicting the effects of jet exhaust plume on three-dimensional (3-D) nozzle-afterbody configurations. The thin-layer Navier-Stokes formulation (ref. 7) was modified to simulate jet mixing problems (ref. 1). The code allows for the partitioning of the flow-field domain into multiblock grids and is capable of using several numerical schemes to solve the governing equations and different turbulence models (ref. 8).

A computational domain can be divided into zones consisting of longitudinal planes that are arranged linearly in the streamwise direction. Each zone is subdivided into blocks that can have different boundary conditions applied at each of their six faces. The four lateral block faces either communicate with adjacent block faces or serve as outer zone boundaries or symmetry planes. The upstream and downstream faces are zone interfaces that are handled similar to the lateral faces. A user-written control file determines the communication between blocks and the

type of boundary condition to be used at each face. Blocks can be partitioned along the streamwise direction to provide for a change in boundary conditions part way along a lateral block face. Different grid topologies for neighboring blocks are permitted, with some restrictions on grid matching at block boundaries. This structure allows relatively complex configurations and flow conditions to be modeled more efficiently. Additionally, the code permits different numerical schemes to be applied selectively to each block, for example, the space-marching technique for supersonic flows and time-dependent calculations for subsonic and separated flows.

### Boundary Conditions

The PAB3D code allows different types of boundary conditions to be applied to any given block face. Solid walls are treated as no-slip adiabatic surfaces, and the block interfaces are  $C0$  continuous. The boundary conditions used for the internal nozzle flow path are the total pressure and the total temperature at the block inflow face. In addition, this particular inflow boundary condition assumes a fluid flow angle normal to the inflow face. The operating NPR of the nozzle and the free-stream static pressure  $p_\infty$  determine the jet total pressure at the inflow face from  $p_{t,j} = (\text{NPR})(p_\infty)$ . The design NPR is calculated from the series of equations shown in appendix A. A typical jet total temperature obtained from the experimental tests is used for all the calculations.

A characteristic boundary condition with Riemann invariants is applied to external inflow and outer lateral boundaries. An extrapolation boundary condition is applied on the downstream outflow face where the nozzle plume exits the computational domain.

### Performance Calculation

Nozzle performance is obtained through the application of the momentum theorem to a control volume surrounding the nozzle (ref. 2). Cheatham, Walker, and Gridley calculated both 2-D and 3-D inviscid nozzle performance using this method (ref. 9). The surface over which the integration of the flow quantities is performed is typically the nozzle exit. The method utilized herein integrates the mass and momentum fluxes and the pressure forces over each incremental cell modeling the nozzle outflow faces through the use of equations (1) and (2):

$$w_p = \sum (\rho \mathbf{U} \cdot \mathbf{n}) \Delta A \quad (1)$$

$$\mathbf{F} = \sum [\rho \mathbf{U} (\mathbf{U} \cdot \mathbf{n}) + (p - p_\infty) \mathbf{n}] \Delta A \quad (2a)$$

$$\mathbf{M} = \mathbf{F} \times \mathbf{R} \quad (2b)$$

where  $\Delta A$  is the outflow area attributed to the incremental cell face and  $\mathbf{R}$  is the moment arm from the reference center to the incremental cell.

Ideal mass-flow rate and thrust are determined from the isentropic flow equations (eqs. (3) and (4)) and are used to normalize the calculated mass-flow rate and thrust for comparisons with the experimental data:

$$w_i = \sqrt{\frac{\gamma}{R}} \left( \frac{2}{\gamma + 1} \right)^{\frac{\gamma+1}{2(\gamma-1)}} A_t \frac{p_{t,j}}{\sqrt{T_{t,j}}} \quad (3)$$

$$F_i = \sqrt{\frac{2\gamma R}{\gamma - 1}} w_p \sqrt{T_{t,j} \left[ 1 - \left( \frac{p_\infty}{p_{t,j}} \right)^{\frac{\gamma-1}{\gamma}} \right]} \quad (4)$$

The performance package is incorporated into PAB3D to permit monitoring of various performance parameters as the solution converges.

## Results and Discussion

Solutions were obtained for four nozzle configurations from the flow method PAB3D. The solutions were all computed with laminar viscous stress modeling due to biasing of the turbulent flow models to a single direction. This modeling obviates turbulence calculations when an H-type grid is used to describe the nozzle geometry. Discharge coefficient, thrust ratio, and off-axis force and moment quantities (where applicable) were calculated for different operating conditions.

### Case 1: Stratford Choke Nozzle Study

A sectional view of the Stratford choke nozzle is shown in figure 2. Gridding arrangements and convergence data are shown in figures 7 to 10. Four computational grids were run for this geometry. Residual trends and discharge coefficient convergence are plotted for each grid.

**Grid definition.** This case study was modeled with two computational zones. The first zone contained the nozzle internal grid and an external grid region surrounding the nozzle, and the second zone modeled the external air downstream of the nozzle exit. The dimensions of the nozzle block were  $129 \times 2 \times 105$ . The nozzle internal-boundary-layer grid region contained 34 points, with the first grid point specified from  $y^+ = 4$ . Grid expansion rates were less than 5 percent in the axial and radial directions. The external region surrounding the nozzle grid was dimensioned at  $129 \times 2 \times 208$ . Total-pressure and total-temperature boundary conditions

were applied to both inflow faces of these blocks. The external downstream region was dimensioned at  $145 \times 2 \times 313$ . The zone interface matched point for point between the two zones. The grid was stretched toward the outer boundary to a distance of 40 exit radii. Solid-wall boundary conditions were applied to this surface. The outflow boundary was 15 exit radii downstream of the nozzle exit plane. Extrapolation boundary conditions were applied to the outflow boundary. Each of the successively coarser grids used grid points from this mesh. A sectional view of the grid in the  $ik$ -plane is shown in figure 7(a). This grid represented the most dense concentration of points for this study. The grid density was reduced by two in both the  $i$ -direction (axial), and  $k$ -direction (radial) three successive times. Figures 8(a), 9(a), and 10(a) are sectional views of grids reduced by  $1/2$ ,  $1/4$ , and  $1/8$ . Grid 1 is the baseline grid. Grids 2, 3, and 4 are the  $1/2$ ,  $1/4$ , and  $1/8$  grids, respectively.

An axisymmetric flow symmetry is assumed through the use of a 2-D wedge-angle boundary condition. A single-cell-width polar grid was generated with a wedge angle of  $5.625^\circ$ , which represents  $1/64$  of an axisymmetric geometry. The wedge-angle boundary condition calculates the angle of the wedge lateral faces and determines the proper boundary values to apply to satisfy the symmetry assumptions.

**Discharge coefficient correlation.** The nozzle pressure ratio for this study was set at 2. The external free stream was initially set at  $M_\infty = 0.05$ . The initial solutions for the time-dependent calculations for grids 2, 3, and 4 were produced through a two-step procedure. A one-dimensional (1-D) isentropic solution was calculated for the nozzle internal grid, as described in appendix B. This flow field was the starting point for a space-marching solution for the jet exhaust downstream of the nozzle exit. Time-dependent calculations were continued on the resulting flow field. The calculation for grid 1 utilized a converged solution from grid 2 extrapolated to the grid 1 computational domain for the starting solution. Residual trends for the four grids are shown in figures 7(b), 8(b), 9(b), and 10(b). Discharge coefficient convergences are shown in figures 7(c), 8(c), 9(c), and 10(c). The effect of grid count on discharge coefficient is shown figure 11.

The discharge coefficient stabilized for grids 2 and 3 within 1000 solution iterations (1 sweep downstream and 1 sweep back upstream by the solver was counted as 1 iteration) and grid 4 stabilized within 600 iterations. There appears to have been no close correlation between the solution residuals and convergence of the calculated nozzle discharge coefficient after the first 1000 iterations. Excursions

of 2 orders of magnitude in the residual were observed, with no discernible change in the discharge coefficient after that point. The discharge coefficient for grid 1 remained stable as well, despite the residual dropping over an order of magnitude over approximately 1000 iterations. Solution residuals were therefore used only as an initial indicator of solution stability (i.e., that the solution is not diverging) and discharge coefficient was utilized as the indicator of final solution convergence.

The effect of grid count of discharge coefficient is shown in figure 11. The very coarse grid (grid 4) of this study converged to 0.5 percent of the level of the experimental data. Grid 3 converged to within 0.1 percent, and grids 2 and 1 were less than 0.1 percent of the experimental discharge coefficient. Discharge coefficient was a stable and convergent quantity with grid count.

## Case 2: Throat Contouring Study

**Grid definition.** Two nozzles (A1 and A2, see fig. 3) with different throat radii were modeled. A representative internal computational grid for a non-axisymmetric nozzle is shown in figure 12(a). The ordinate of the plot was nondimensionalized by the length of the divergent flap, with the origin at the nozzle throat. The computational grid for the nozzle was an H-H grid consisting of 61 grid points in the  $i$ -direction (axial), 49 points in the  $j$ -direction (lateral), and 37 grid points in the  $k$ -direction (vertical). The grid spacing of the internal grid mesh was packed in the boundary layer near the walls and stretched away in the center region of the nozzle. Flow symmetry was assumed about the horizontal and vertical planes to reduce computational time. The number of cells was identical for both nozzle configurations.

The nozzle internal-boundary-layer grid region contained 13 grid points, with the first grid point specified as 0.00003 cm from the wall surface. This region was roughly 0.115 cm deep in the  $k$ -direction along the divergent flaps and 0.251 cm deep in the  $j$ -direction along the sidewalls at the nozzle exit (exit half-height was roughly 1.5 cm). Constant-interval spacing from the boundary-layer edge to the centerline was used for the remaining grid points.

In the calculation of off-design settings (i.e., underexpanded nozzle flow), the static external air was modeled to allow the jet plume to adjust to the jump in static pressure that occurred near the nozzle exit face. The external and internal domains were split into three zones, as shown in figures 12(b) and 12(c). The first zone ( $61 \times 49 \times 37$ ) contained the nozzle internal geometry, which was the same as

in the single-zone case. The second ( $8 \times 87 \times 73$ ) and third ( $17 \times 44 \times 37$ ) zones were free-stream domains, with the second zone serving as a transition between the denser nozzle geometry grid and the relatively sparse grid of the third zone. This transition avoided radical grid changes, such as the 2:1 grid reduction at the boundary to the second and third zones, in areas of possibly high flow gradients such as those expected to occur at the nozzle exit. A representative grid arrangement for the first  $i$ -plane of the second zone is shown in figure 12(d). A cut in this zone face matched point for point the nozzle exit grid of the last  $i$ -plane in the first zone. The grid was stretched toward the outer boundaries at a distance of five equivalent nozzle radii away from the outer line of the matching cut. The code required about 4 million words of memory for the execution of the multizone cases (approximately 190 000 grid points).

A 1-D isentropic solution described in appendix B was used for the starting flow field. Mass flow of the nozzle was observed to gauge solution convergence.

**Pressure data correlation.** The computed nozzle internal pressures for nozzles A1 and A2, which are presented in figure 13, compared well with experimental data. These solutions converged within about 400 time steps that took roughly 3100 sec on the Cray-2 computer with an initial Courant-Friedrichs-Lewy (CFL) stability number of 3. The CFL numbers for subsequent iterations during a run are adjusted automatically within the code to accelerate convergence.

The ability to calculate the change in nozzle flow due to a difference in throat radius (static pressure distribution of nozzle A1 subtracted from that of nozzle A2) is shown in figure 14. The magnitude and location of the incremental pressure differences due to the change in nozzle throat radius were fairly well matched. This pressure difference integrated over the length of the divergent flaps (i.e.,  $x/l_s > 0$ ) was 1.58 N, or roughly an increment of 0.002 in thrust ratio based on ideal thrust (from the ideal mass flow). The pressure gradients across the exit were lower for nozzle A2 than for nozzle A1, probably because of the weaker pressure gradients between the divergent flaps of nozzle A2. The magnitude of the pressure force at the exit (subtracted from the free-stream static pressure) was much smaller for nozzle A2 than for A1 ( $-0.47$  N compared with  $-11.12$  N). It appears that nozzle A2 was operating closer to the theoretical design conditions than nozzle A1 was operating for the same input total-pressure conditions because of the smaller loss of thrust to pressure forces.

**Nozzle performance.** The discharge coefficient converged to within 0.5 percent of the experimental data level. This level of convergence was typical for this particular set of single-zone calculations of the nozzle internal flow.

As shown in figure 15, the agreement of the computed and the experimental discharge coefficient was within experimental accuracy for both nozzles. Figure 16 shows the comparison of calculated and measured internal thrust ratios for the range of NPR's tested for nozzles A1 and A2. The calculated on-design ( $NPR_d = 2.97$ ) thrust ratio was 0.6 percent high for nozzle A1 and 1.1 percent high for nozzle A2 as compared with the experimental data. This comparison was relatively consistent over the range of NPR's from design to 8.0. Laminar viscous stress modeling could have contributed to excess thrust being calculated because a boundary layer that was thinner than actual was calculated along the divergent flaps.

With a Reynolds number based on the equivalent throat radius (approximately  $1.28 \times 10^6$ ), laminar (from Blasius' equation) and turbulent (from ref. 10, p. 636) boundary-layer profiles were calculated for flow over a flat plate for a distance equal to the length of the nozzle divergent flaps. A portion of these profiles and the velocity distribution at the exit plane calculated by PAB3D for nozzle A1 are shown in figure 17. As would be expected from a flow calculation using laminar viscous stresses in PAB3D, the laminar-flat-plate distribution more closely matched the boundary layer calculated by PAB3D than did the turbulent-flat-plate profile. The laminar-boundary-layer thickness occupied roughly 2 percent of the nozzle semi-height at the exit. A similar calculation using a turbulent flow model resulted in a boundary-layer thickness of almost 9 percent of the nozzle exit semi-height. The velocity distribution along the upper divergent flap showed several regions of reversed flow, as shown in figure 18. The first boundary-layer reattachment, a few centimeters downstream of the throat, was a likely location of the transition to turbulent flow. Therefore, the actual boundary-layer thickness at the nozzle exit may have been slightly thinner than that of the turbulent flow estimate, but thicker than that of just the laminar calculation. A thicker boundary layer on the nozzle divergent flaps would result in lower computed values of thrust.

The difference in performance between nozzles A1 and A2 is shown in figure 19 for experimental and theoretical results. The difference in experimental nozzle thrust performance due to the change in throat radius was statistically zero, as the variance in

performance was less than the experimental data accuracy of 0.5 percent. Similar small increments were computed by PAB3D for the range of NPR's from design to 8.0.

### Case 3: Translating Sidewall Yaw Vectoring Study

A cross-sectional sketch of the translating sidewall yaw vectoring concept of reference 5 is shown in figure 4. Effective yaw vector angle was experimentally measured for five sidewall positions at several NPR settings. The performance validation for this set of nozzle geometries cut across the experimental data two ways. The first fixed the geometry at one sidewall position, with calculations made for three pressure ratios: design NPR ( $NPR_d = 2.967$ ), and NPR = 5.0 and 8.0. The second was made on geometries of varying sidewall cutback positions, with the nozzle operating at a constant NPR = 5.0. The quarter-plane symmetric-flow model could no longer be used because of the generation of unbalanced off-axis (i.e., yawing) forces. The generation of side forces with no net normal forces would have required this symmetry boundary to be placed in the horizontal plane cutting through the center of the model.

**Grid definition.** The computational grid was split into 4 streamwise zones, with the first zone containing 2 blocks and the remaining 3 zones containing 10 blocks each. A representative sketch of the grid is shown in figure 20. A quarter-plane cross-sectional cut of the grid at the nozzle exit plane and the blocking strategy are shown in figures 20(c) and 20(d). Blocks 1 and 2 in zone 1 modeled the internal flow path containing  $41 \times 49 \times 37$  grid points, each using an H-H topology. The cross-plane and boundary-layer grid was similar to that used for case 2. More densely packed grid is placed in the external lateral sidewall region, where the vectored flow could exhaust into the static free stream. All the external blocks used H-O grid topology.

**Performance calculation.** Calculation of effective yaw vector angle required the determination of both the axial force and the side force generated by the nozzle flow. Integration of the momentum fluxes and the shearing forces across the nozzle exit face and the cutaway part of the sidewall accounted for all the vectoring forces. The prediction of the change in effective yaw vector angle with NPR for a fixed sidewall cutback position is shown in figure 21. Prediction of the change in effective yaw vector angle with sidewall position for a fixed NPR is shown in figure 22.

Overall, the trend and the level of effective yaw vector angle were predicted to within  $0.5^\circ$  of the experimental data over the range of NPR's for nozzle S3 ( $(x_s - x_t)/l_s = 0.25$ ). The static pressure at the nozzle exit is lower than the free-stream static pressure when operating at overexpanded conditions. This pressure difference caused air to be drawn into the nozzle passage through the cutback sidewall; hence, the sign of the effective yaw vector angle at the low NPR was reversed. Operating the nozzle at design conditions resulted in a slightly positive yaw vector angle because of a small amount of flow outward through the sidewall cutout. The zero point for the effective yaw vector angle would have occurred at some operating condition between design NPR and an overexpanded NPR, where the momentum fluxes creating side forces balanced out across the available outflow surfaces of the nozzle.

The change in effective yaw vector angle with sidewall cutback was predicted to within  $0.3^\circ$  over the range of sidewall positions at  $\text{NPR} = 5.0$ . (See fig. 22.) Along with the integration of the momenta flux and pressure forces in the lateral direction through the sidewall cutout, the shearing forces across the exit face must be included to account for all the sideward forces. The shearing forces for nozzle S3 contributed 75 percent of the total side force generated by the nozzle. Similarly, the axially directed shearing forces along the open sidewall face contributed roughly 10 percent to the thrust of the nozzle.

#### Case 4: Multiaxis Thrust Vectoring Study

The axisymmetric nozzle geometries reported by Carson and Capone (ref. 6) consisted of designs for two power settings and two flap lengths. (See fig. 5.) The short-flap, dry power nozzle with  $\text{NPR}_d = 5.01$  ( $\epsilon = 1.350$ ) was chosen for this set of comparisons. This nozzle was tested at four geometric pitch vector angles ( $\delta_{v,p} = 0^\circ, 10^\circ, 20^\circ$ , and  $30^\circ$ ) and one combined pitch-yaw vectoring mode ( $\delta_{v,p} = 14^\circ, \delta_{v,y} = 14^\circ$ ). A sectional sketch of the nozzle internal shape for the different pitch vector angles is shown in figure 6. Yawing and pitching moments along with mass flow and axial thrust were experimentally measured. The moments were nondimensionalized by the ideal axial thrust and a reference length. The reference length was the nozzle throat diameter, 5.756 cm, and the moment reference center was the center of the force balance, 24.765 cm upstream of the nozzle connect station. Predicted and experimental data are presented for the nozzle operating at the design NPR.

**Grid definition.** The prediction of the off-axis forces required a gridding of the geometry with no assumed planes of symmetry. The computational domain was divided into two zones, with two blocks in each zone for the nozzle split laterally. An oblique view of the cell-centered grid is shown in figure 23(a). The grid in the centerline plane is shown in figure 23(b) for the nozzle vectored  $0^\circ$  and in figure 23(c) for the nozzle vectored  $30^\circ$ . The first zone, with each block dimensioned  $28 \times 17 \times 17$ , extended from just upstream of the physical nozzle connect station to the beginning of the convergent section before the throat. The second zone, with each block dimensioned  $45 \times 33 \times 33$ , consisted of the convergent and divergent sections of the nozzle ending at the nozzle exit plane. Each block had an H-O grid topology, as shown in figures 23(c) and 23(d). An extrapolation boundary condition applied to the exit face allowed for terminating the computational volume at that point for calculations of flow at on-design nozzle pressure ratios.

**Performance calculation.** Experimental data and various calculated performance quantities for four different configurations are shown in figures 24 to 27. The numerical schemes used for solutions for this geometry were first order in the  $j$ -direction and third order in the  $i$ - and  $k$ -directions. All five configurations were run using laminar flow assumptions. Nozzle mass flow was determined from the statistical average of the mass flow through the first 18  $i$ -planes of the first zone. The moments and forces generated by the nozzle flow were obtained through the integration of the fluid momentum flux, pressure, and shearing forces at the exit plane.

The level of and the increment in discharge coefficient with change in the geometric pitch vector angle were predicted to within experimental accuracy at the design nozzle pressure ratio of 5.01. (See fig. 24.) Losses due to the sharp throat contour kept  $w_p/w_i$  at around 0.95 for  $\delta_{v,p} = 0^\circ$  and  $10^\circ$ . Gradually larger losses were predicted for the higher vectoring angles.

The change in thrust ratio with varying geometric pitch angle was predicted to within 2 percent of the experimental data at the design nozzle pressure ratio, as shown in figure 25. The change in pitching moment with varying geometric pitch vector angle was similarly predicted, as shown in figure 26.

The capability of predicting multiaxis thrust vectoring is shown in figure 27 for the following three configurations:  $\delta_{v,p} = 0^\circ, \delta_{v,y} = 0^\circ$ ;  $\delta_{v,p} = 20^\circ, \delta_{v,y} = 0^\circ$ ; and  $\delta_{v,p} = 14^\circ, \delta_{v,y} = 14^\circ$ . Experimentally, the combined pitch-yaw thrust vectoring case was generated by a  $45^\circ$  rotation about the

centerline axis at the nozzle connect station of the nozzle with  $20^\circ$  of pitch vectoring. Exactly the same methodology was numerically applied to the analytical description of the  $20^\circ$  pitch vector geometry to produce the combined pitch-yaw computational grid. Numerically the yawing moments predicted for the  $\delta_{v,y} = 0^\circ$  geometries were zero. The predicted yawing moment for the combined pitch-yaw geometry was within 0.7 percent of the experimental data (fig. 27(b)). Similar agreement of experimental data with predicted pitching moment is shown in figure 27(a). The relative levels of pitching moment were within 1 percent of experimental levels, and in particular the loss of pitching moment due to rotation of the pitch axis by  $45^\circ$  was predicted.

## Conclusions

A nozzle internal performance module has been written and incorporated into a three-dimensional Navier-Stokes solver PAB3D for the calculation of nozzle internal performance. The flow quantities calculated are discharge coefficient; normal, side, and axial thrust ratios; rolling, pitching, and yawing moments; and effective pitch and yaw vector angles. The calculations were compared with experimental data from several investigations performed in the static test facility of the Langley 16-Foot Transonic Tunnel. The results are summarized as follows:

1. Nozzle discharge coefficient was predicted to within experimental accuracy over a range of nozzle pressure ratios from design to underexpanded pressure ratios.
2. The effect of throat contour geometry on nozzle discharge coefficient and thrust ratio was predicted over a range of nozzle pressure ratios for a two-dimensional convergent-divergent nozzle.
3. The effect of sidewall cutback on the effective yaw vector angle generated by a two-dimensional convergent-divergent nozzle operating at an underexpanded pressure ratio was predicted typically to within  $0.5^\circ$  of the experimental data. The effect of varying nozzle pressure ratio from overexpanded to underexpanded conditions on effective yaw vector angle for a fixed sidewall cutback position was also predicted typically to within 0.5 percent of the experimental data.
4. Thrust vectoring forces and moments were predicted typically within 2 percent of experimental data for an axisymmetric multiaxis thrust vectoring nozzle operating at the design nozzle pressure ratio.

NASA Langley Research Center  
Hampton, VA 23681-0001  
August 13, 1992

## Appendix A

### Calculation of Design Nozzle Pressure Ratio

The physical geometry of a nozzle fixes the nozzle pressure ratio (NPR) at which the most efficient operation of the nozzle occurs. The following equations are used to determine the design NPR when the nozzle expansion ratio  $\epsilon$  is known.

The inverse of the nozzle expansion ratio is the ratio of the nozzle throat area to the nozzle exit area:

$$\frac{A_t}{A_e} = \frac{1}{\epsilon} \quad (\text{A1})$$

The nozzle exit Mach number (isentropic) is solved

by using a Newton iterative method on the following equation:

$$\frac{A^*}{A} = \left( \frac{\gamma + 1}{2} \right)^{\frac{\gamma+1}{2(\gamma-1)}} M_d \left( 1 + \frac{\gamma - 1}{2} M_d^2 \right)^{\frac{-\gamma+1}{2(\gamma-1)}} \quad (\text{A2})$$

where  $\frac{A_t}{A_e}$  is used for  $\frac{A^*}{A}$ . The ratio  $\frac{p}{p_t}$  is calculated from the Mach number:

$$\frac{p}{p_t} = \left( 1 + \frac{\gamma - 1}{2} M_d^2 \right)^{\frac{-\gamma}{\gamma-1}} \quad (\text{A3a})$$

The inverse of  $\frac{p}{p_t}$  is the design pressure ratio of the nozzle:

$$\text{NPR}_d = \frac{1}{p/p_t} \quad (\text{A3b})$$

## Appendix B

### Calculation of Initial Flow-Field Solutions

A starting Mach number distribution is determined from the area distribution of the internal geometry  $\left(\frac{A_t}{A}\right)$  using equation (A2) and assuming sonic conditions at the throat. The dimensionless ratios of temperature and pressure are then calculated from the Mach number distribution interpolated to cell-centered coordinates with the following 1-D isentropic relations:

$$\frac{T}{T_t} = \left(1 + \frac{\gamma - 1}{2} M_l^2\right)^{-1} \quad (\text{B1})$$

$$\frac{p}{p_t} = \left(1 + \frac{\gamma - 1}{2} M_l^2\right)^{\frac{-\gamma}{\gamma - 1}} \quad (\text{B2})$$

Typical scale-model operating jet total-pressure and total-temperature levels are chosen to calculate

the quantities  $\rho$ ,  $u$ , and  $e$  with the following equations:

$$T = T_{t,j} \frac{T}{T_t} \quad (\text{B3})$$

$$p = p_{t,j} \frac{p}{p_t} \quad (\text{B4})$$

$$\rho = \frac{p}{RT} \quad (\text{B5})$$

$$a = \sqrt{\gamma RT} \quad (\text{B6})$$

$$u = a M_l \quad (\text{B7})$$

$$e = \frac{1}{2} \rho u^2 + \frac{p}{\gamma - 1} \quad (\text{B8})$$

Each plane of cells ( $i = \text{Constant}$ ) is uniformly assigned these quantities. The initial solution assumes the cross-components of velocity (e.g.,  $v$  and  $w$ ) are zero. The flow variables  $\rho$ ,  $\rho u$ ,  $\rho v$ ,  $\rho w$ , and  $e$  are then written to the restart file of the code and utilized as the initial solution.

## References

1. Abdol-Hamid, Khaled S.: The Application of 3D Marching Scheme for the Prediction of Supersonic Free Jets. AIAA-89-2897, July 1989.
2. Kuchemann, Dietrich; and Weber, Johanna: *Aerodynamics of Propulsion*, First ed. McGraw-Hill Book Co., Inc., 1953.
3. Stratford, B. S.: The Calculation of the Discharge Coefficient of Profiled Choked Nozzles and the Optimum Profile for Absolute Air Flow Measurement. *J. Royal Aeronaut. Soc.*, vol. 68, no. 640, Apr. 1964, pp. 237–245.
4. Mason, Mary L.; Putnam, Lawrence E.; and Re, Richard J.: *The Effect of Throat Contouring on Two-Dimensional Converging-Diverging Nozzles at Static Conditions*. NASA TP-1704, 1980.
5. Mason, Mary L.; and Berrier, Bobby L.: *Static Investigation of Several Yaw Vectoring Concepts on Nonaxisymmetric Nozzles*. NASA TP-2432, 1985.
6. Carson, George T., Jr.; and Capone, Francis J.: *Static Internal Performance of an Axisymmetric Nozzle With Multiaxis Thrust-Vectoring Capability*. NASA TM-4237, 1991.
7. Newsome, Richard W.; Walters, Robert W.; and Thomas, James L.: An Efficient Iteration Strategy for Upwind/Relaxation Solutions to the Thin-Layer Navier-Stokes Equations. *A Collection of Technical Papers—AIAA 8th Computational Fluid Dynamics Conference*, June 1987, pp. 126–142. (Available as AIAA-87-1113.)
8. Abdol-Hamid, Khaled S.; and Compton, William B., III: Supersonic Navier-Stokes Simulations of Turbulent Afterbody Flows. *A Collection of Technical Papers—AIAA 7th Applied Aerodynamics Conference*, American Inst. of Aeronautics and Astronautics, July–Aug. 1989, pp. 268–277. (Available as AIAA-89-2194-CP.)
9. Cheatham, P. L.; Walker, S. H.; and Gridley, M. C.: Computation of Vectoring Nozzle Performance. AIAA-90-2752, July 1990.
10. Schlichting, Hermann (J. Kestin, transl.): *Boundary-Layer Theory*, Seventh ed. McGraw-Hill Book Co., c.1979.

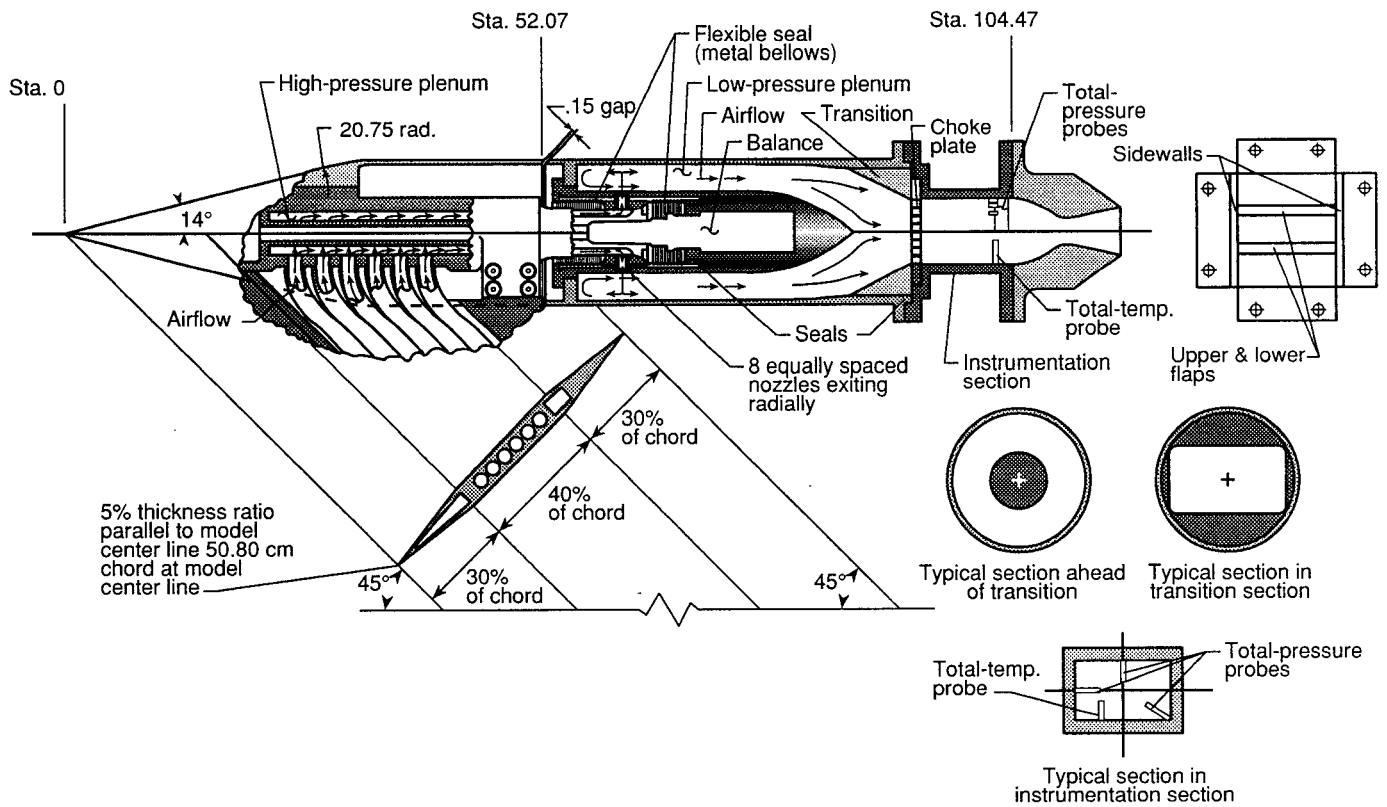


Figure 1. Air-powered nacelle model with typical nozzle configuration installed. Dimensions are in inches unless otherwise noted. (From ref. 4.)

STRATFORD CHOKE NOZZLES								
MEASURED THROAT AREA (IN. <sup>2</sup> )	DESIGN GEOMETRY							
	R <sub>1</sub> , IN.	R <sub>2</sub> , IN.	X, IN.	D <sub>t</sub> , IN.	D <sub>2</sub> , IN.	L <sub>1</sub> , IN.	l, IN.	L <sub>2</sub> , IN.
0.999	2.257	21.314	9.428	1.128	1.378	5.500	11.88	0.903
1.933	3.140	9.000	6.274	1.569	1.820	4.000	9.00	1.623
3.002	3.909	14.715	7.450	1.955	2.204	4.500	9.00	1.564
3.992	4.510	8.320	5.837	2.255	2.505	4.000	9.00	2.052
5.711	5.400	7.700	5.432	2.700	2.950	4.000	9.00	2.239
8.501	6.580	7.868	4.985	3.290	3.540	4.000	9.00	2.270
11.352	7.600	5.900	4.086	3.800	4.050	3.500	9.00	2.300

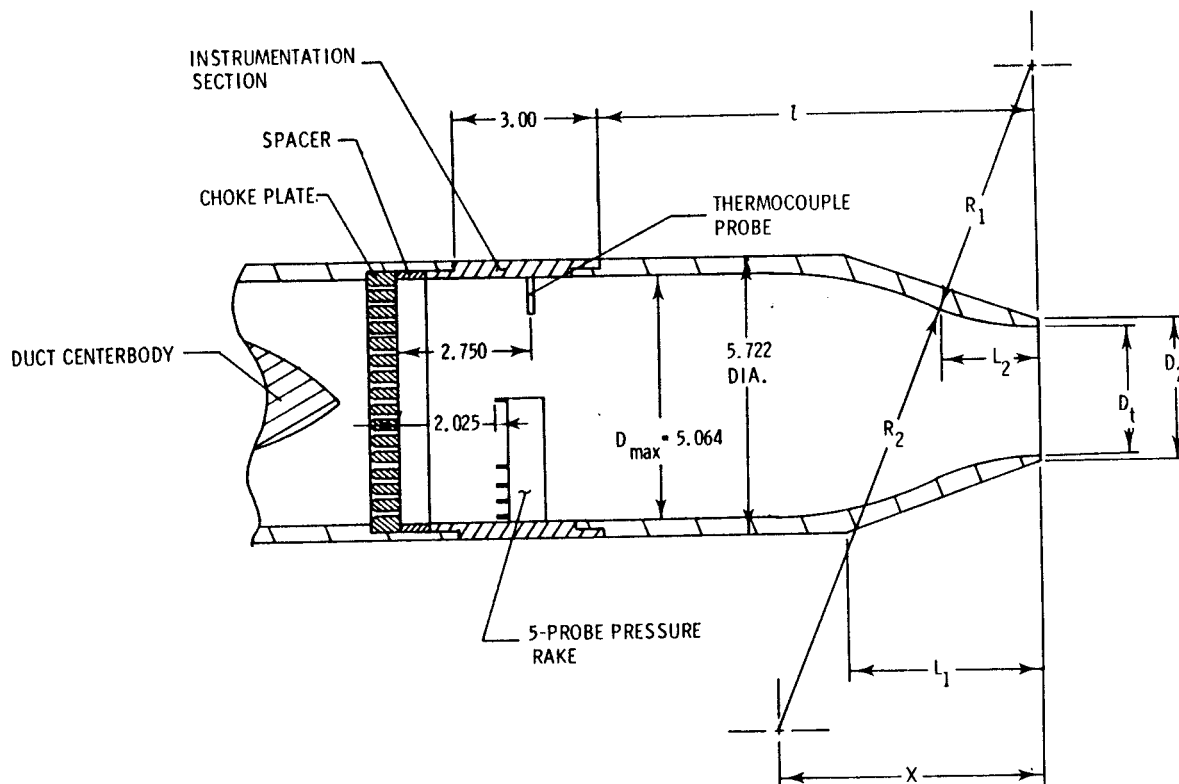
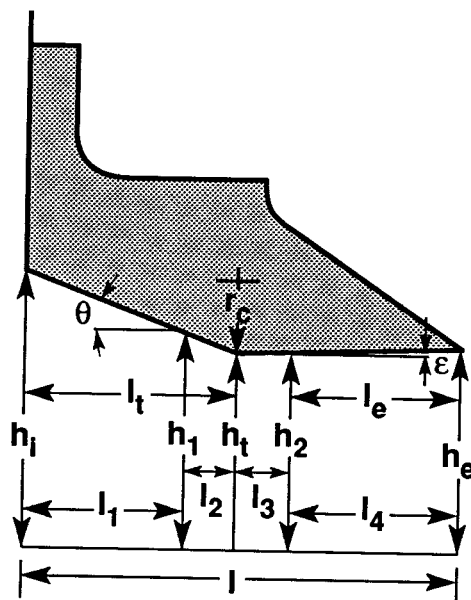


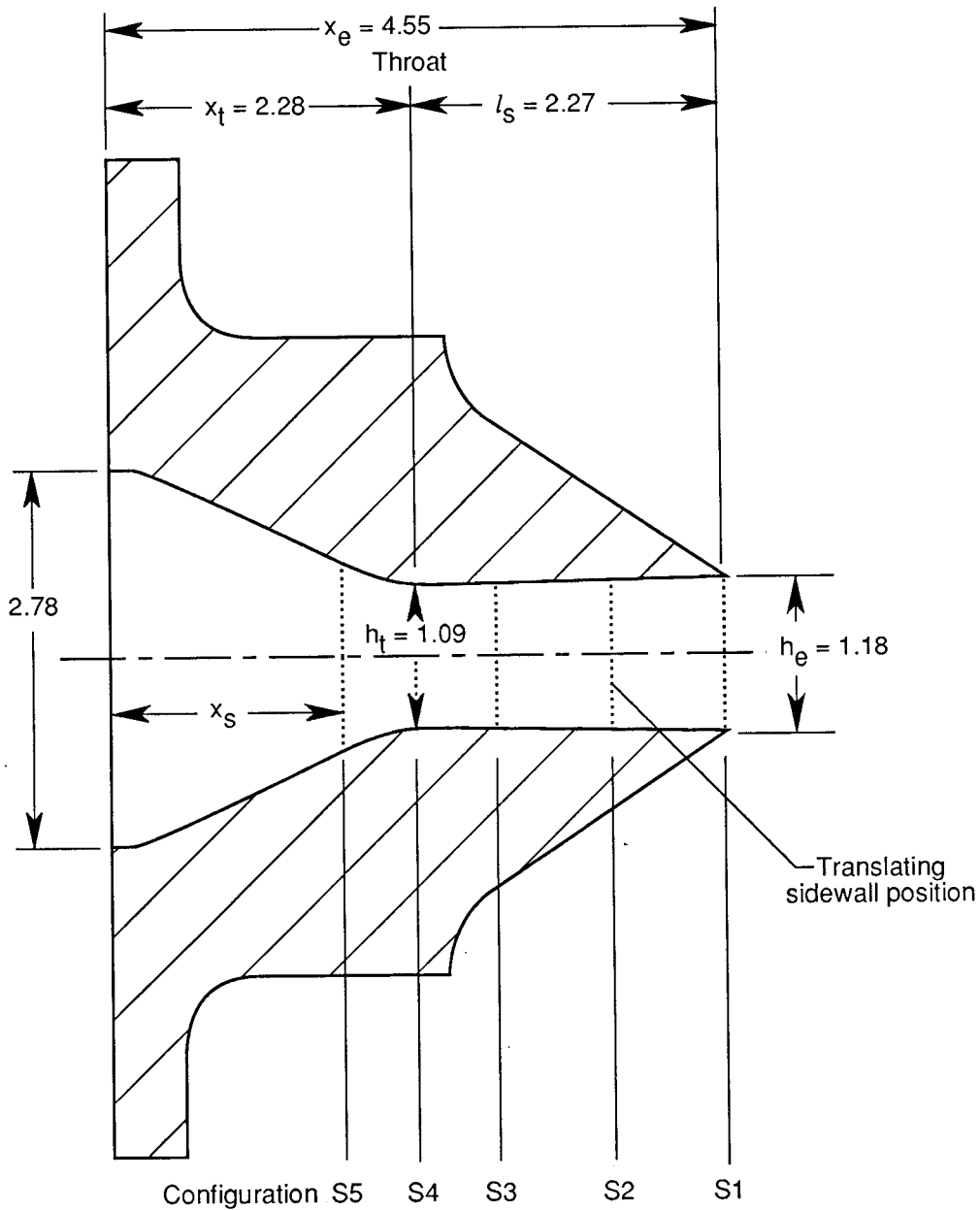
Figure 2. Geometries of Stratford choke nozzle (case 1). Dimensions are in inches.

Sta. 104.47



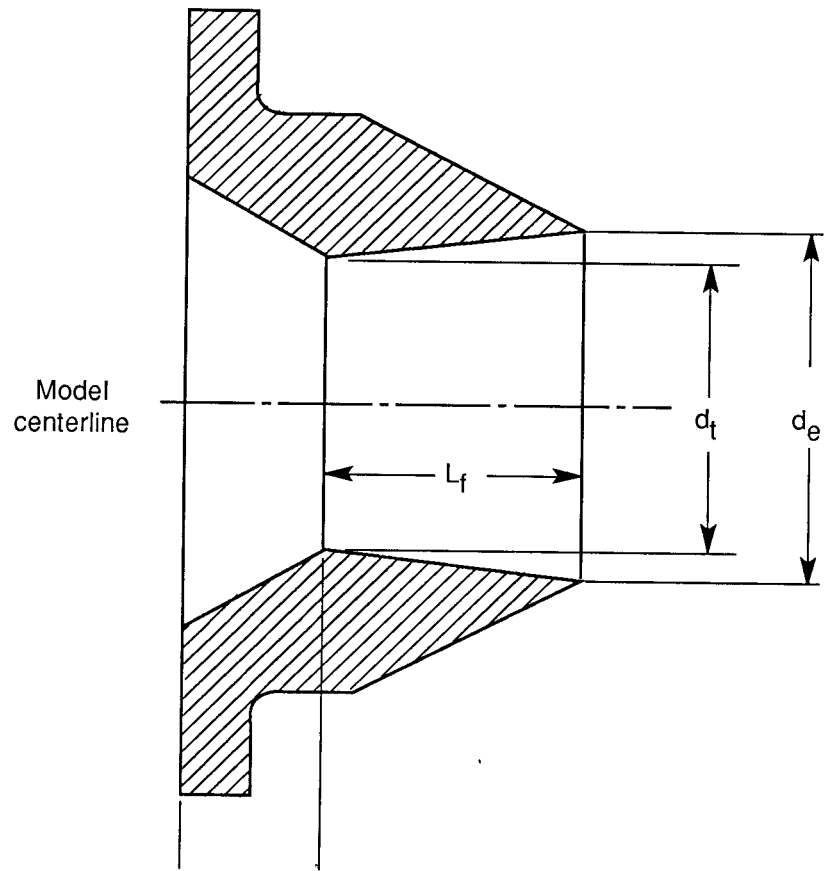
Parameter	A1	A2	Parameter	A1	A2
$A_e, \text{cm}^2$	30.29	30.29	$l_t$	5.78	5.78
$A_t, \text{cm}^2$	27.81	27.81	$l_1$	5.54	4.74
$A_e/A_t$	1.09	1.09	$l_2$	0.24	1.04
$h_e$	1.49	1.49	$l_3$	0.01	0.06
$h_i$	3.52	3.52	$l_4$	5.76	5.72
$h_t$	1.37	1.37	$M_d$	1.35	1.35
$h_1$	1.41	1.57	$\text{NPR}_d$	2.97	2.97
$h_2$	1.37	1.37	$r_c$	0.68	2.74
$l$	11.56	11.56	$\theta, \text{deg}$	20.84	22.33
$l_e$	5.78	5.78	$\epsilon, \text{deg}$	1.21	1.21

Figure 3. Nonaxisymmetric convergent-divergent nozzle configurations (case 2). Dimensions are in centimeters unless otherwise noted. (From ref. 4.)



Configuration	$A_t, \text{in}^2$	$A_e, \text{in}^2$	$A_e/A_t$	AR	$\delta_{v,p}, \text{deg}$	$x_s, \text{in.}$	$(x_s - x_t)/l_s$
S1	4.36	4.72	1.08	3.67	0	4.55	1.00
S2	↓	-	-	↓	↓	3.70	0.63
S3	↓	-	-	↓	↓	2.85	0.25
S4	↓	-	-	↓	↓	2.28	0.00
S5	4.98	-	-	-	↓	1.70	-0.25

Figure 4. Nonaxisymmetric convergent-divergent configuration with translating sidewall yaw vectoring concept (case 3). Dimensions are in inches. (From ref. 5.)



Sta. 42.79    Sta. 43.85 Dry power nozzles  
 Sta. 43.99 Afterburning power nozzles

[ $NPR_d = 5.01$ ;  $A_e/A_t = 1.35$ ]

Power setting	Flap	$A_t, \text{in}^2$	$A_e, \text{in}^2$	$d_t, \text{in.}$	$d_e, \text{in.}$	$L_f, \text{in.}$	$L_f/d_t$
Dry	Short	4.03	5.44	2.266	2.633	1.992	0.88
Dry	Long	4.03	5.44	2.266	2.633	2.994	1.32
Afterburning	Short	7.49	10.11	3.088	3.088	1.984	.64
Afterburning	Long	7.49	10.11	3.088	3.088	2.990	.97

Figure 5. Unvectored axisymmetric nozzle (case 4). (From ref. 6.)

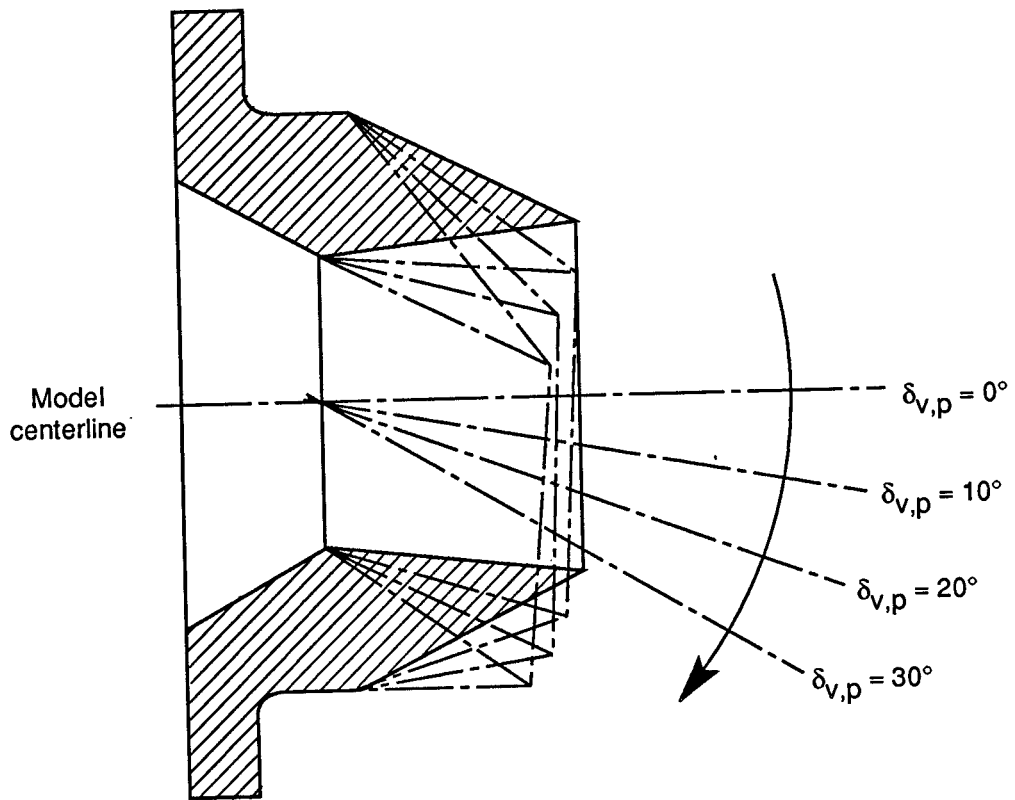
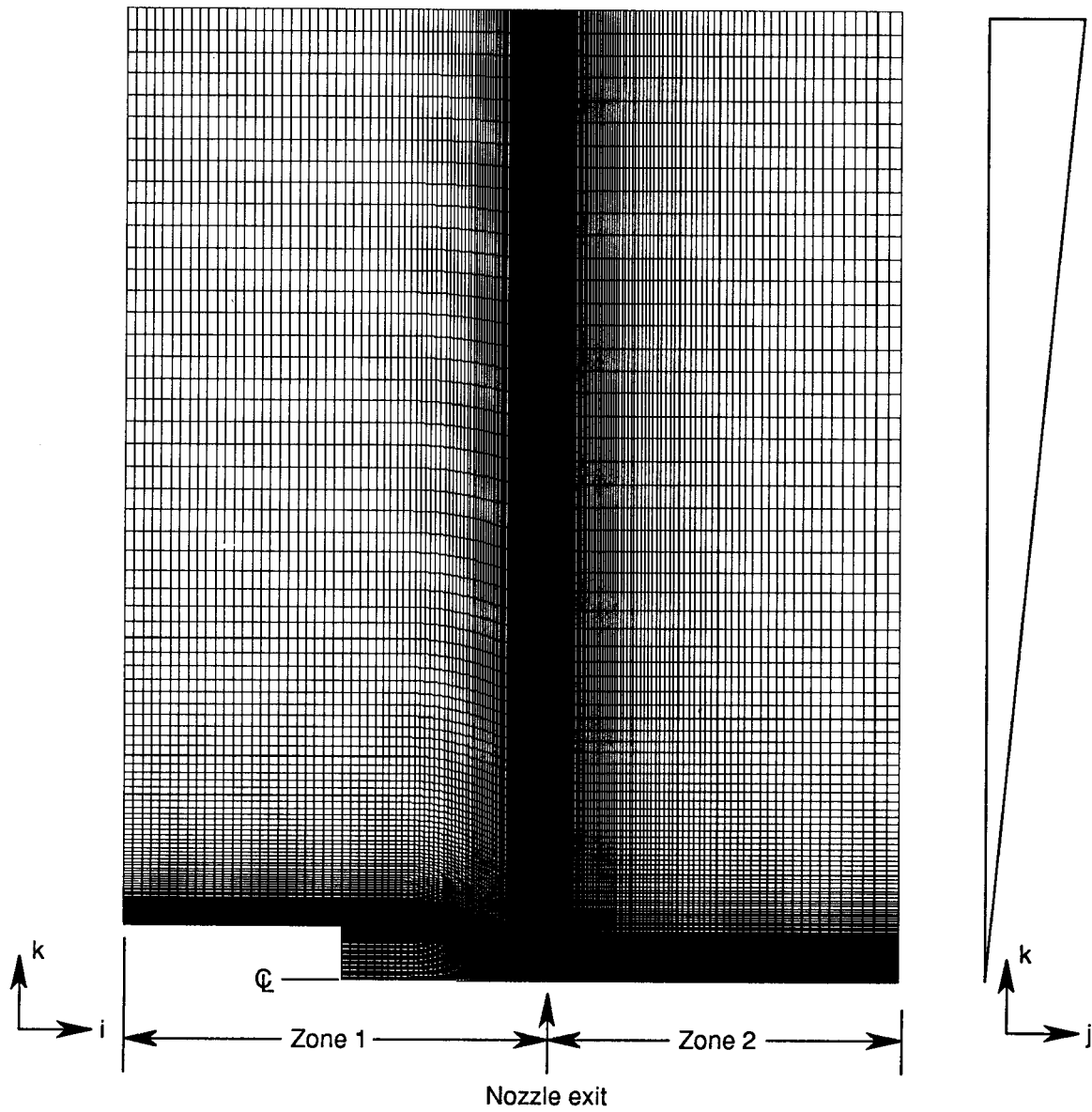
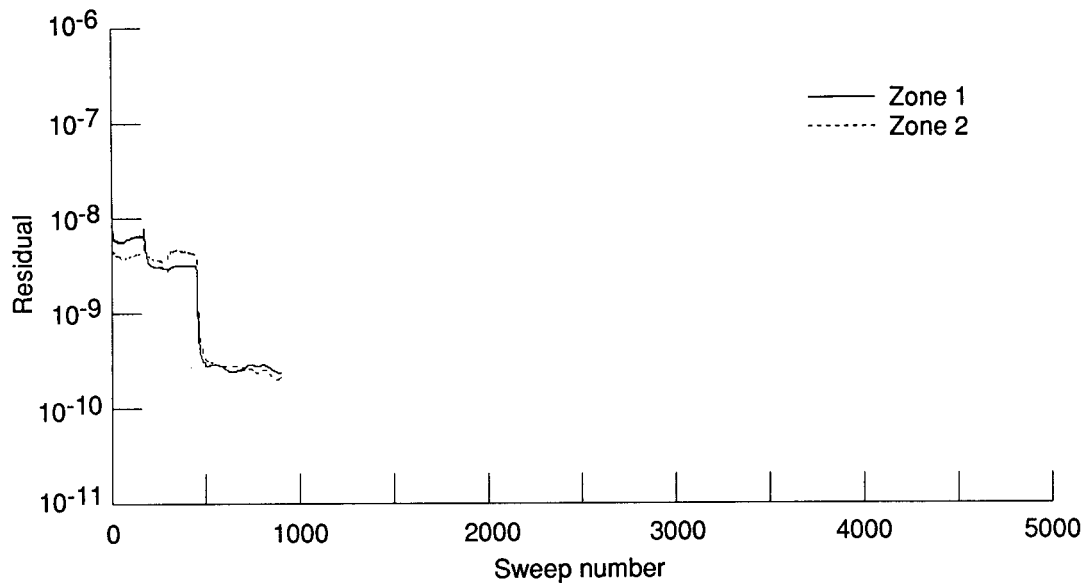


Figure 6. Axisymmetric vectoring nozzle at various thrust vectoring angles. (From ref. 6.)

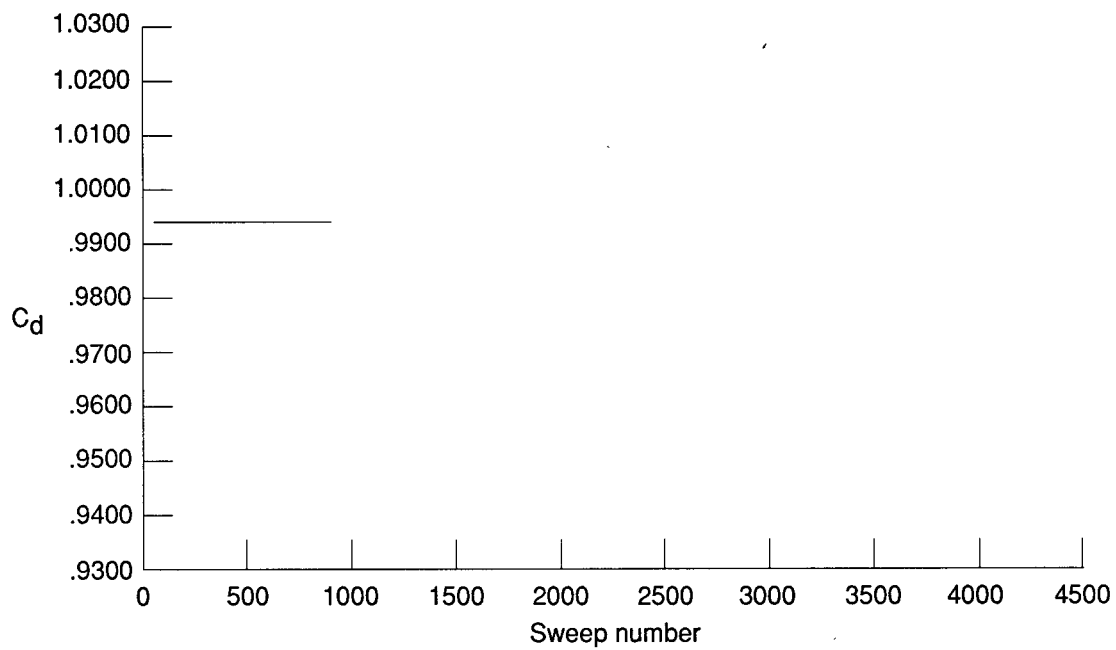


(a) Grid showing  $ik$ -plane.

Figure 7. Baseline grid density of Stratford choke nozzle (case 1.)

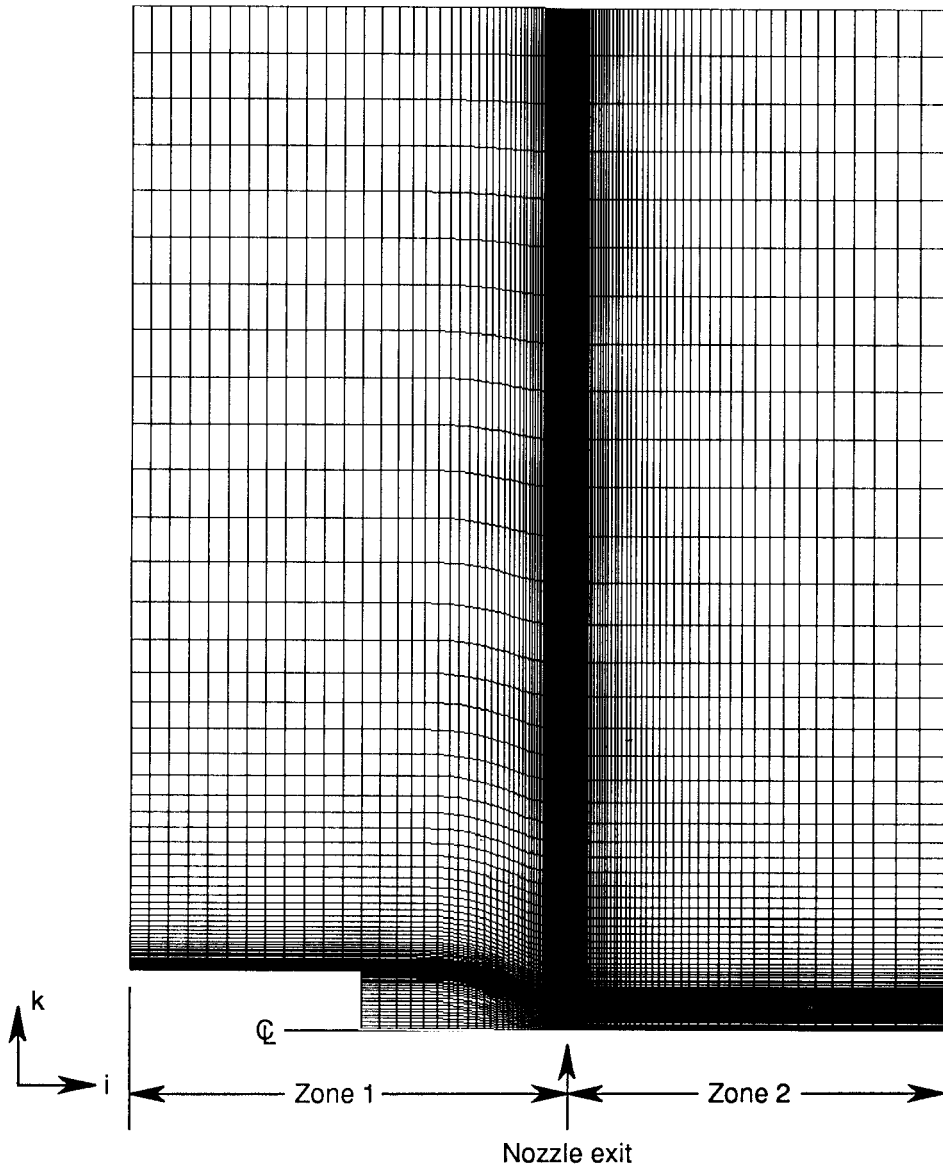


(b) Variation of solution residual with solution sweep number.



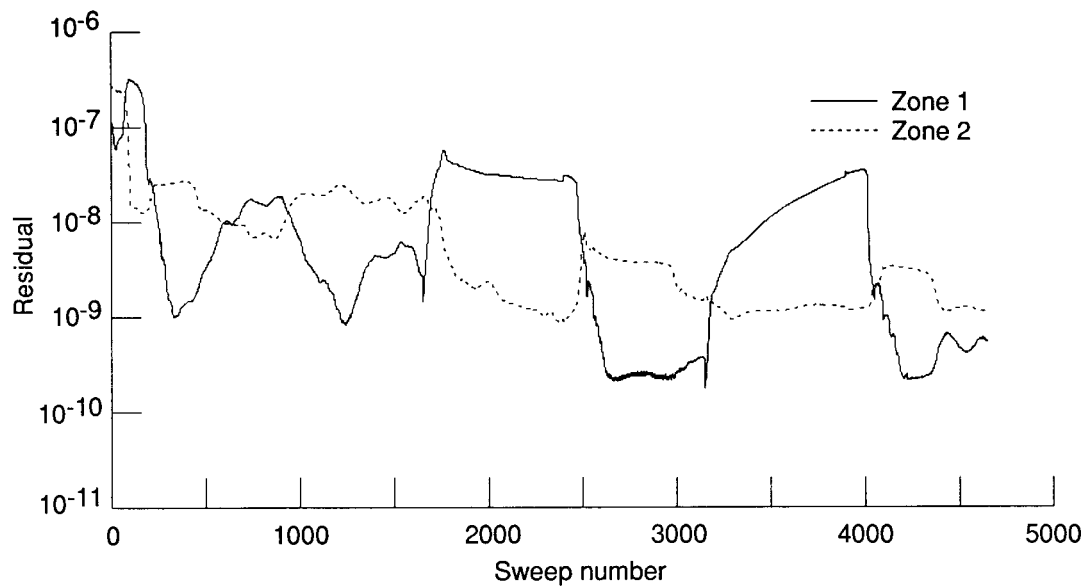
(c) Convergence of discharge coefficient with solution sweep number.

Figure 7. Concluded.

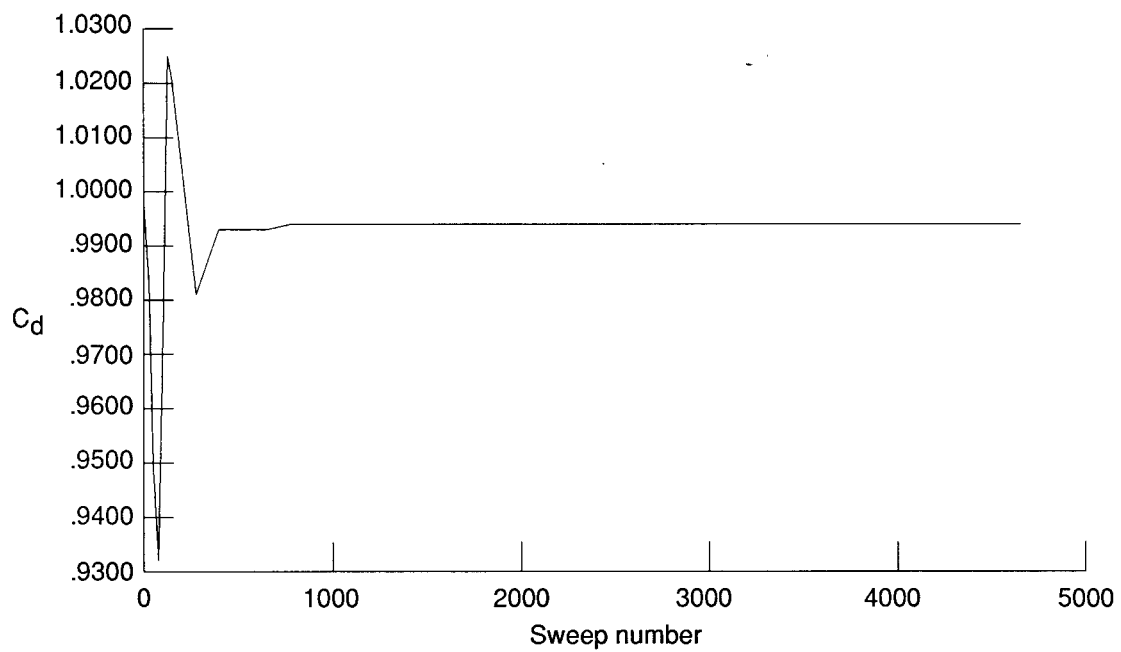


(a) Grid showing  $ik$ -plane.

Figure 8. Grid density reduction of  $1/2$  for Stratford choke nozzle (case 1).

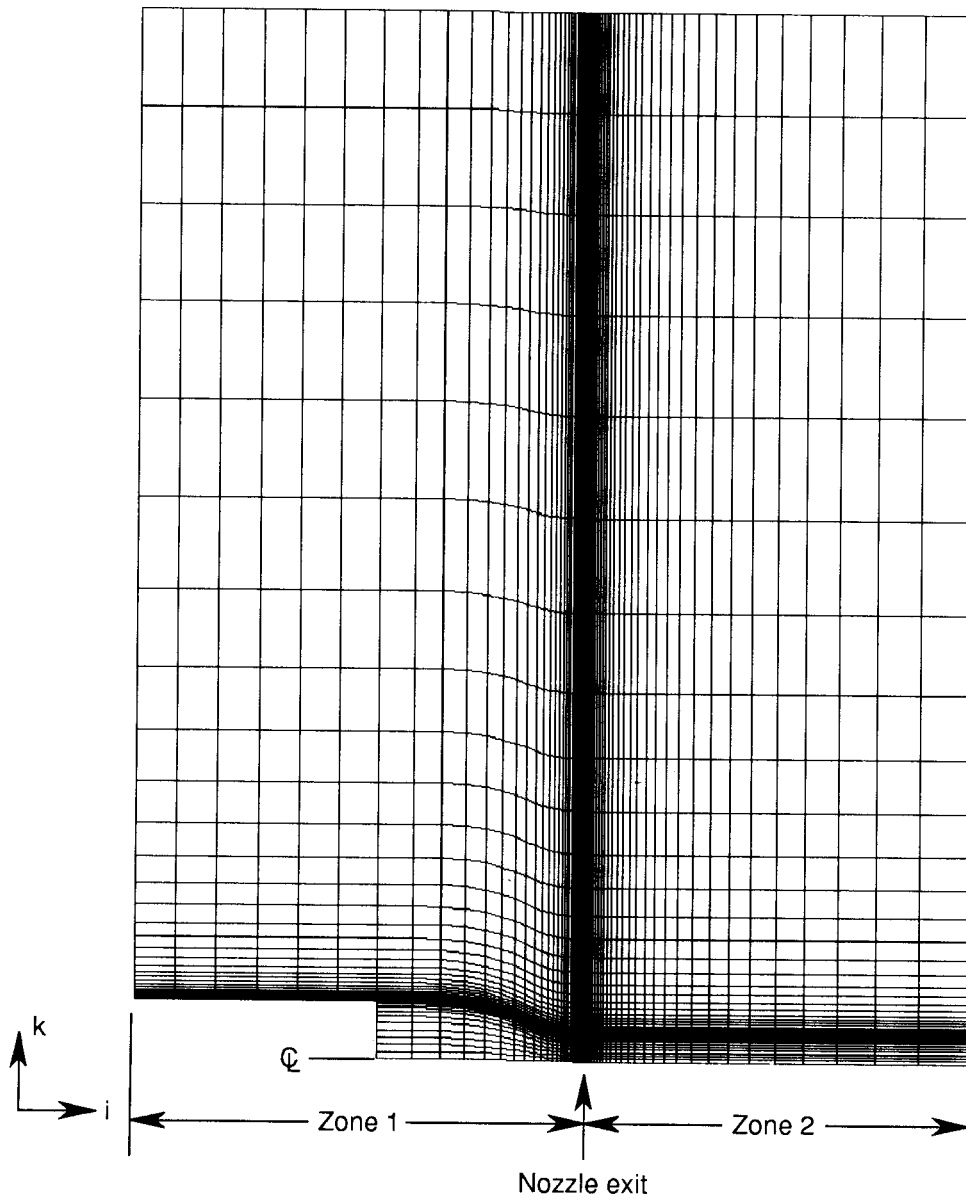


(b) Variation of solution residual with solution sweep number.



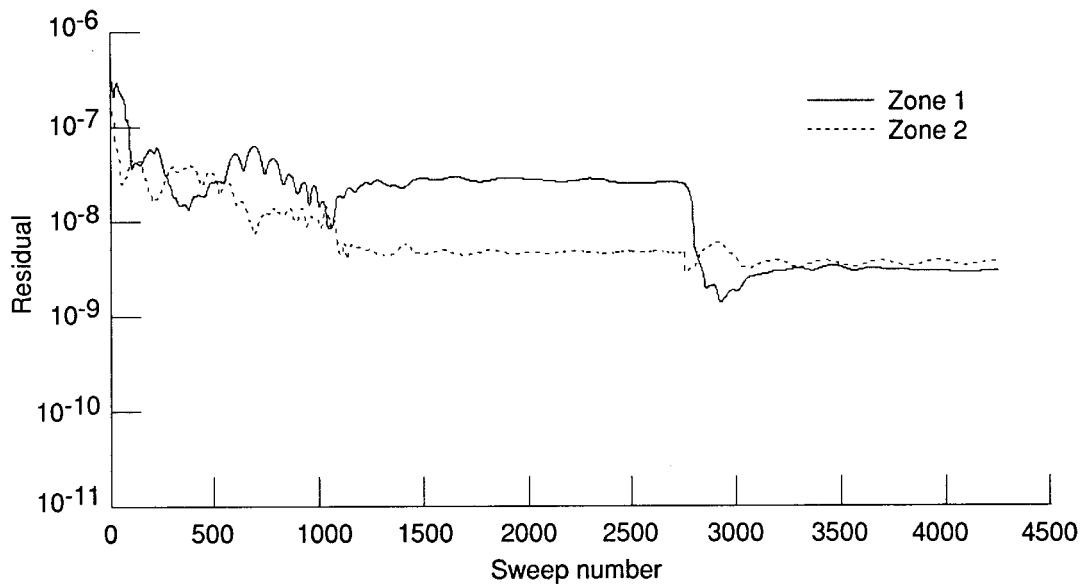
(c) Convergence of discharge coefficient with solution sweep number.

Figure 8. Concluded.

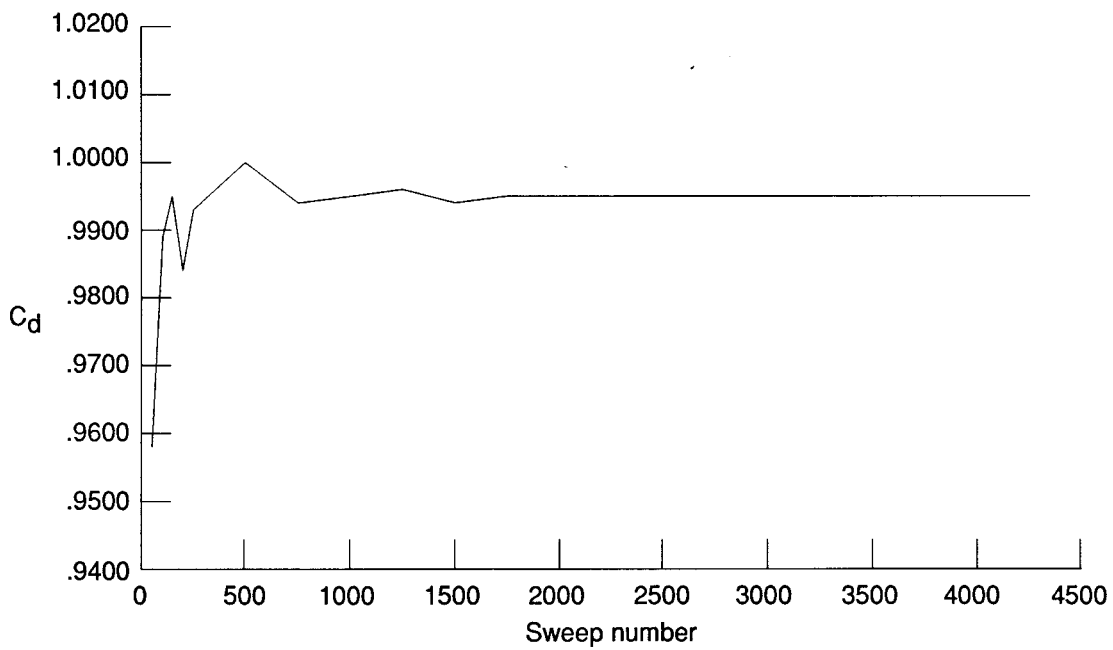


(a) Grid showing  $ik$ -plane.

Figure 9. Grid density reduction of  $1/4$  for Stratford choke nozzle (case 1).

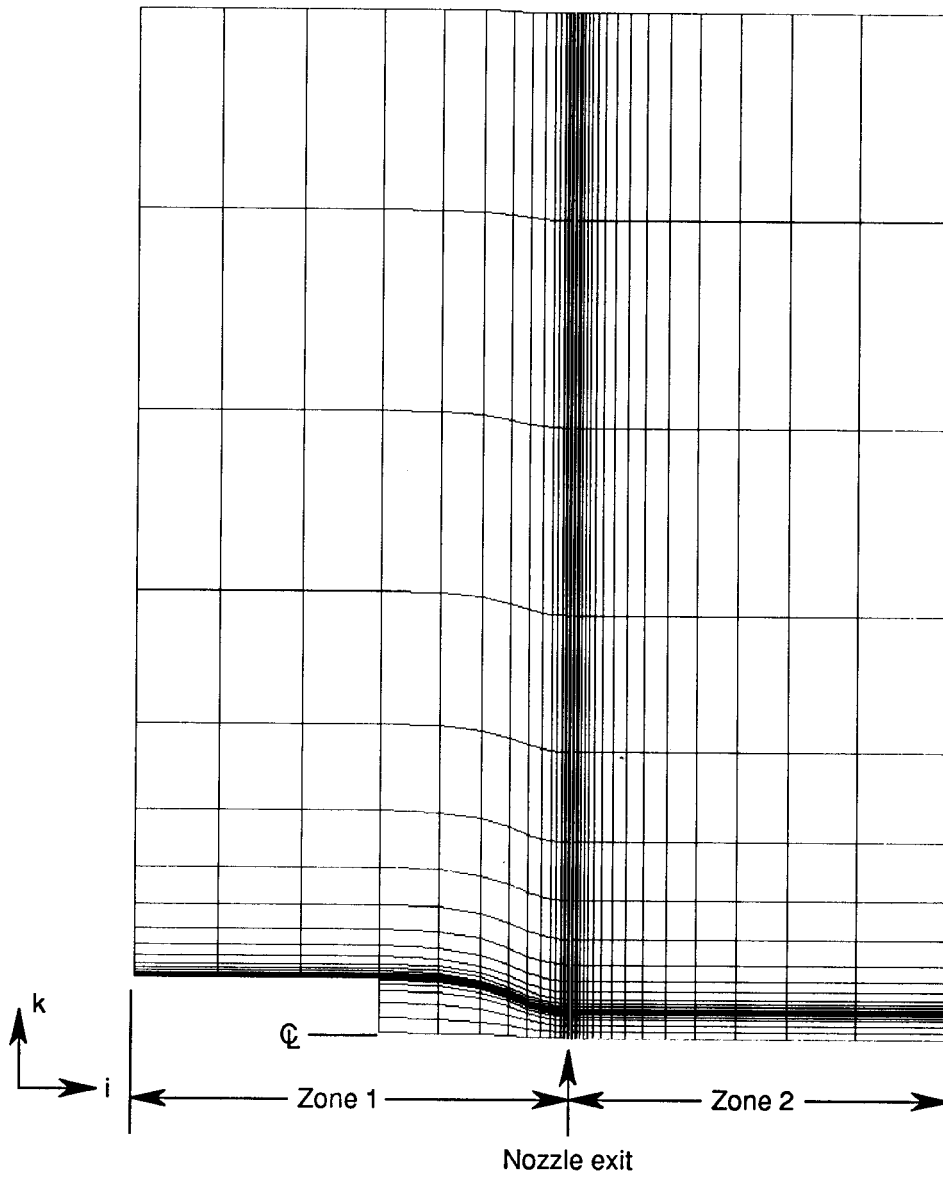


(b) Variation of solution residual with solution sweep number.



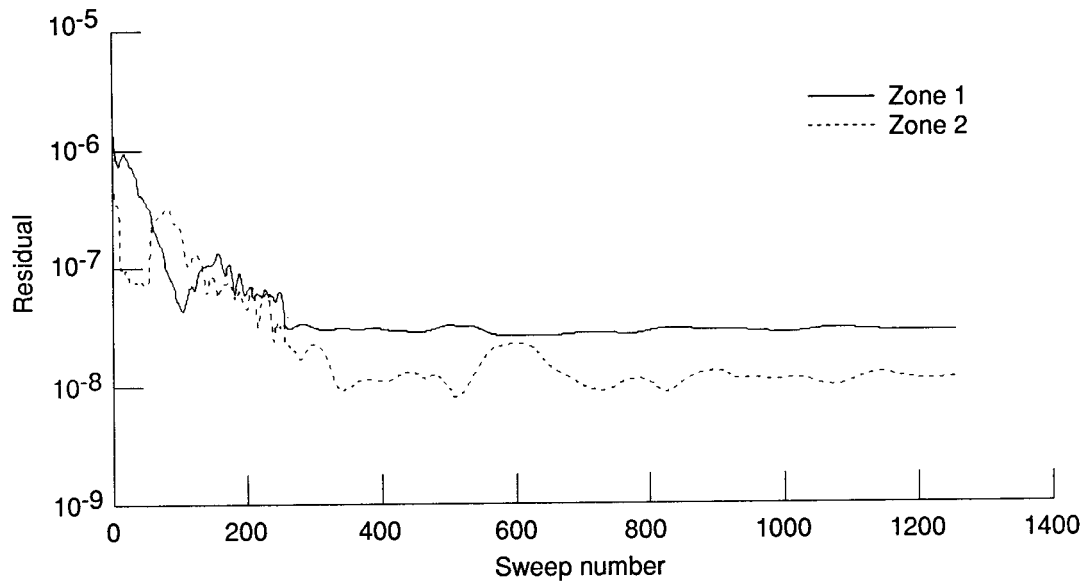
(c) Convergence of discharge coefficient with solution sweep number.

Figure 9. Concluded.

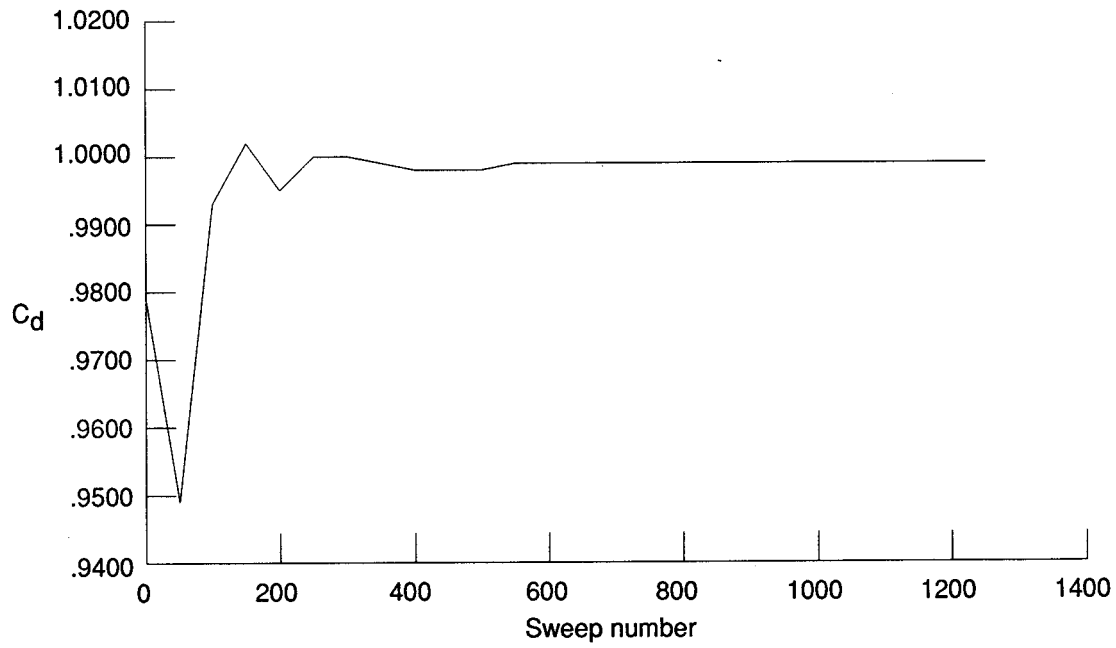


(a) Grid showing  $ik$ -plane.

Figure 10. Grid density reduction of  $1/8$  for Stratford choke nozzle (case 1).



(b) Variation of solution residual with solution sweep number.



(c) Convergence of discharge coefficient with solution sweep number.

Figure 10. Concluded.

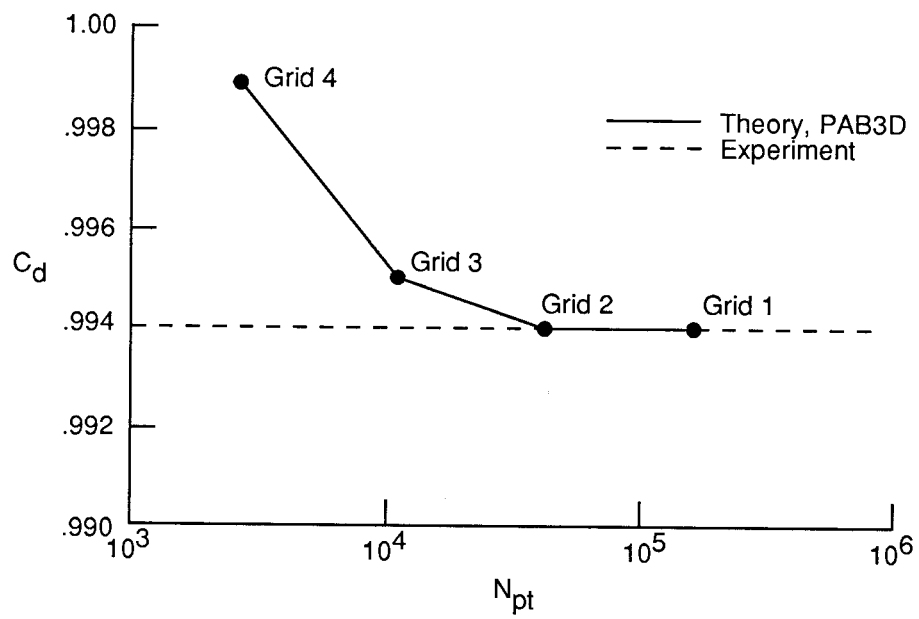
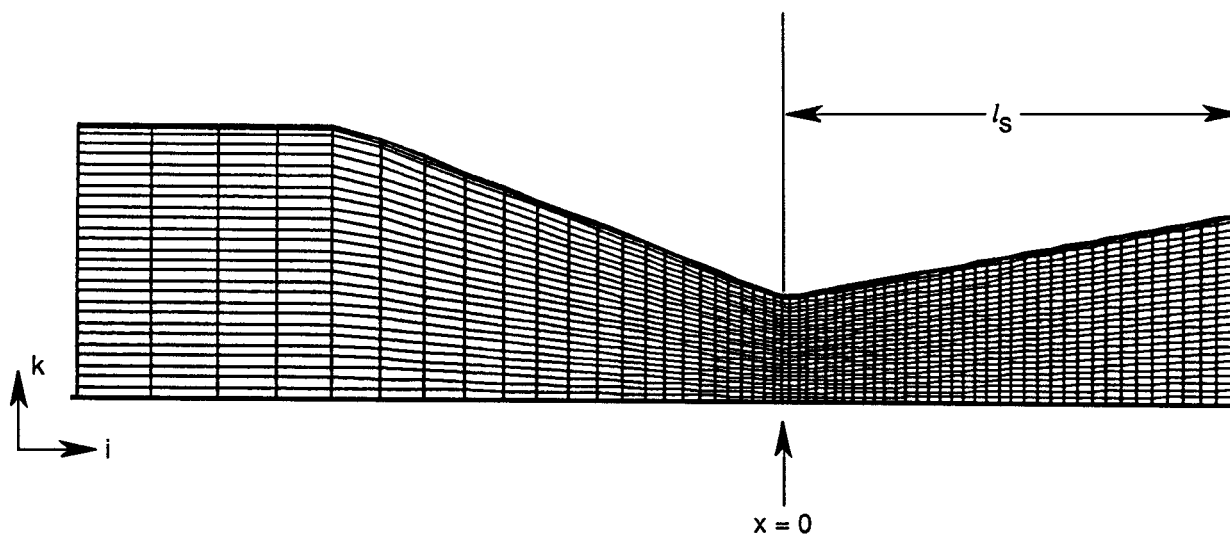
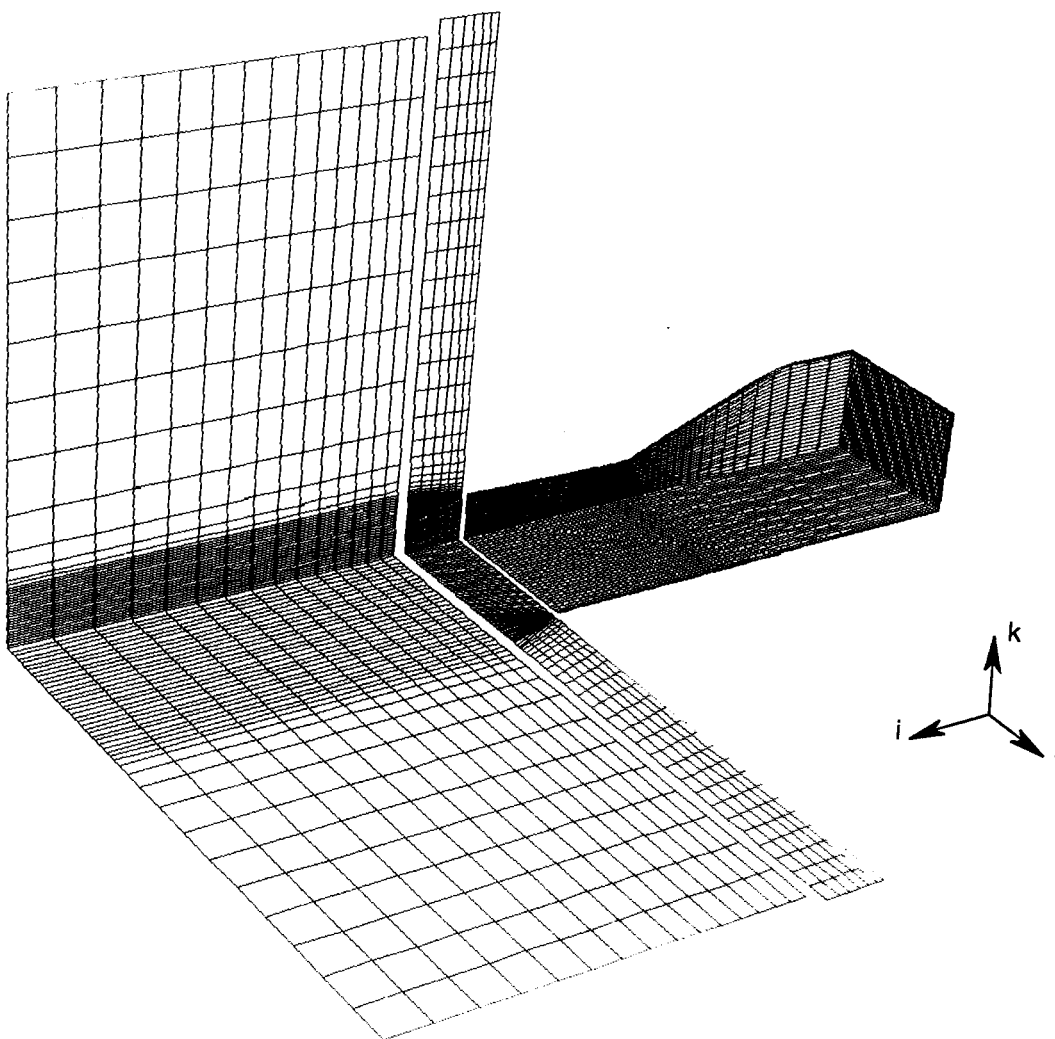


Figure 11. Variation of discharge coefficient with total grid count for case 1.

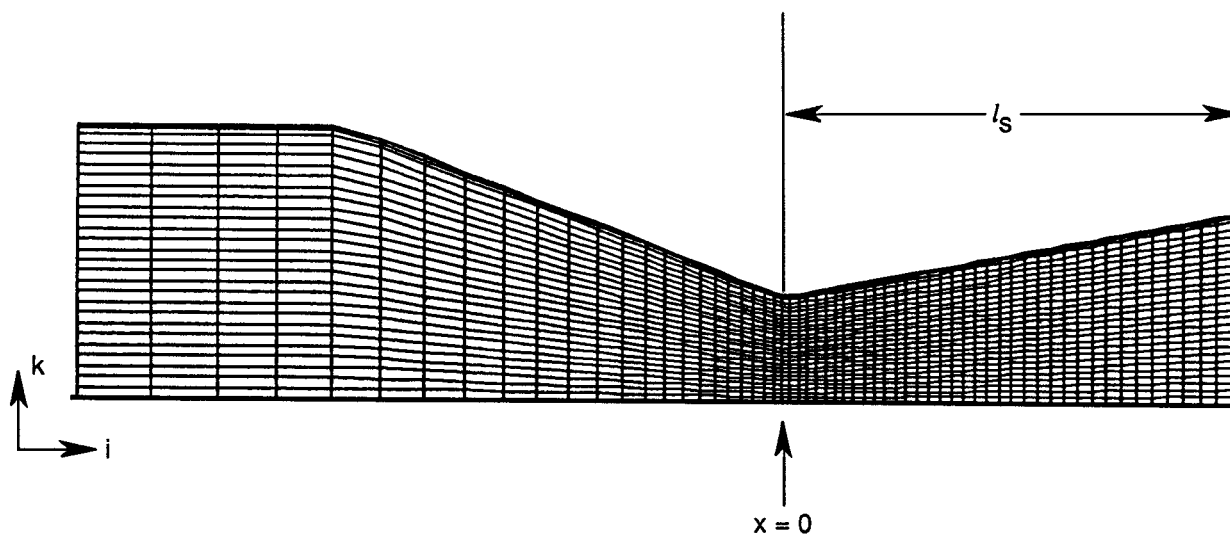


(a) Single-zone geometry showing centerline  $ik$ -plane of nozzle internal shape.

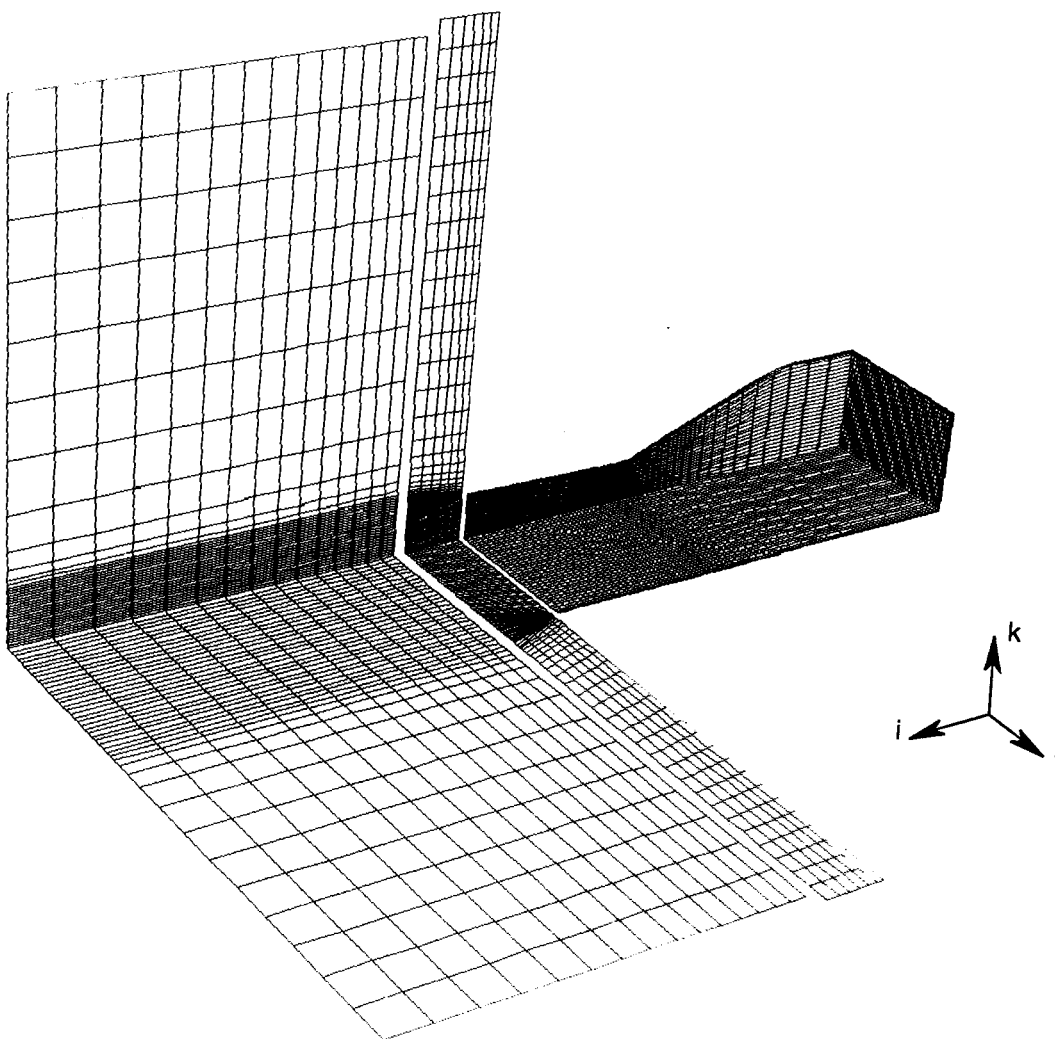


(b) Oblique view of nozzle internal and external cell-centered computational domains.

Figure 12. Grid for nozzle throat contouring study (case 2).

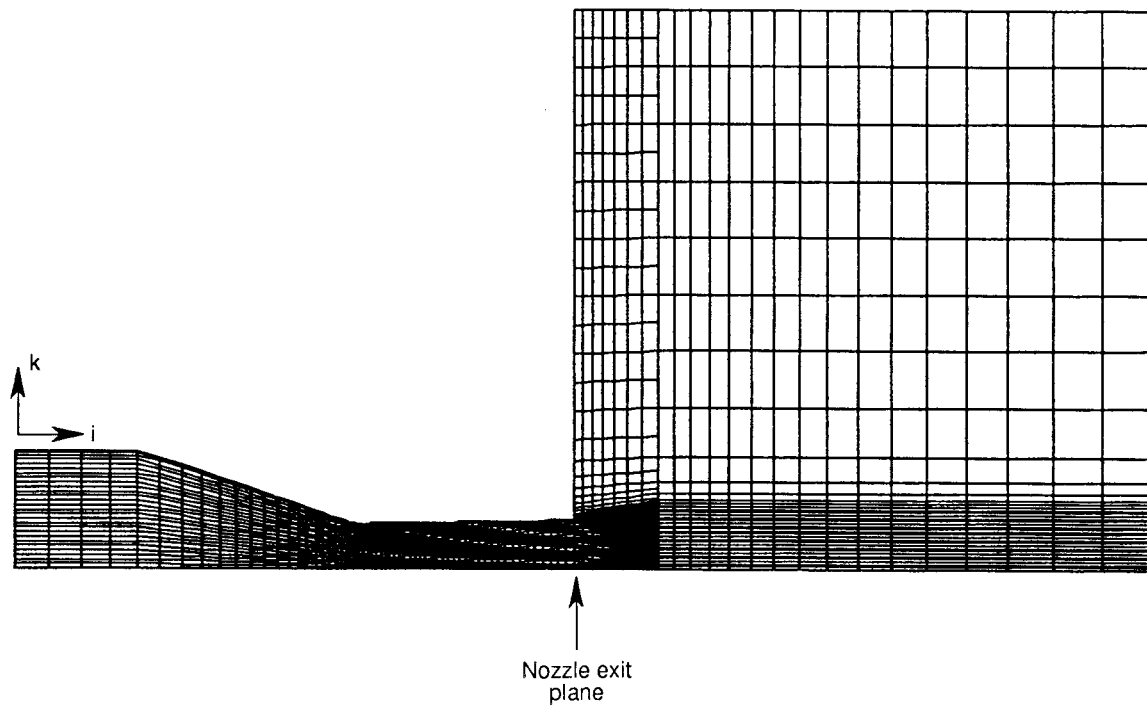


(a) Single-zone geometry showing centerline  $ik$ -plane of nozzle internal shape.

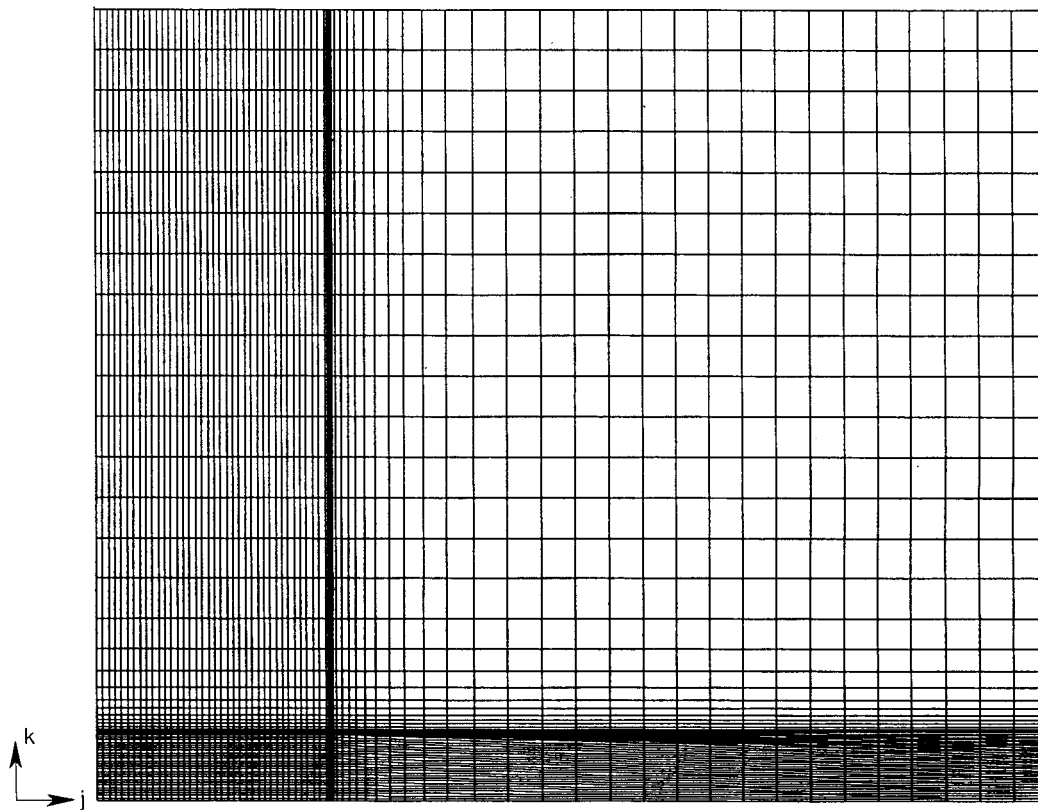


(b) Oblique view of nozzle internal and external cell-centered computational domains.

Figure 12. Grid for nozzle throat contouring study (case 2).

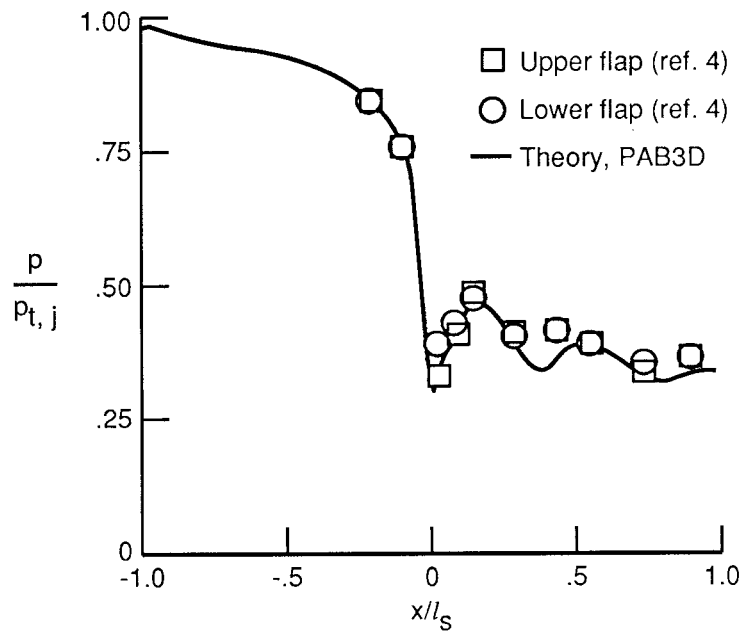


(c) Multizone geometry showing centerline  $ik$ -plane of nozzle internal and external computational domains.

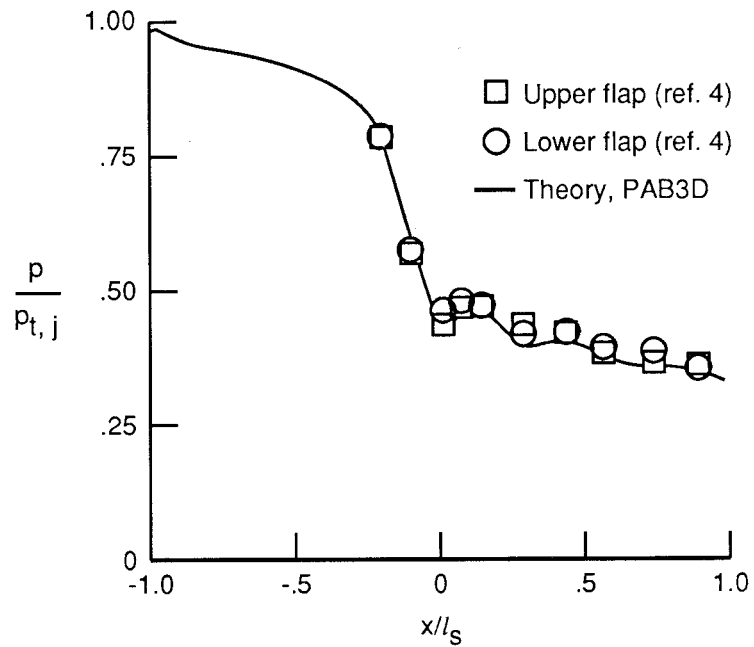


(d) Multizone geometry showing upstream  $jk$ -plane of second zone.

Figure 12. Concluded.



(a) Nozzle configuration A1.



(b) Nozzle configuration A2.

Figure 13. Static pressure distributions of theory and experiment on upper-flap centerline for case 2. Dry power; design NPR.

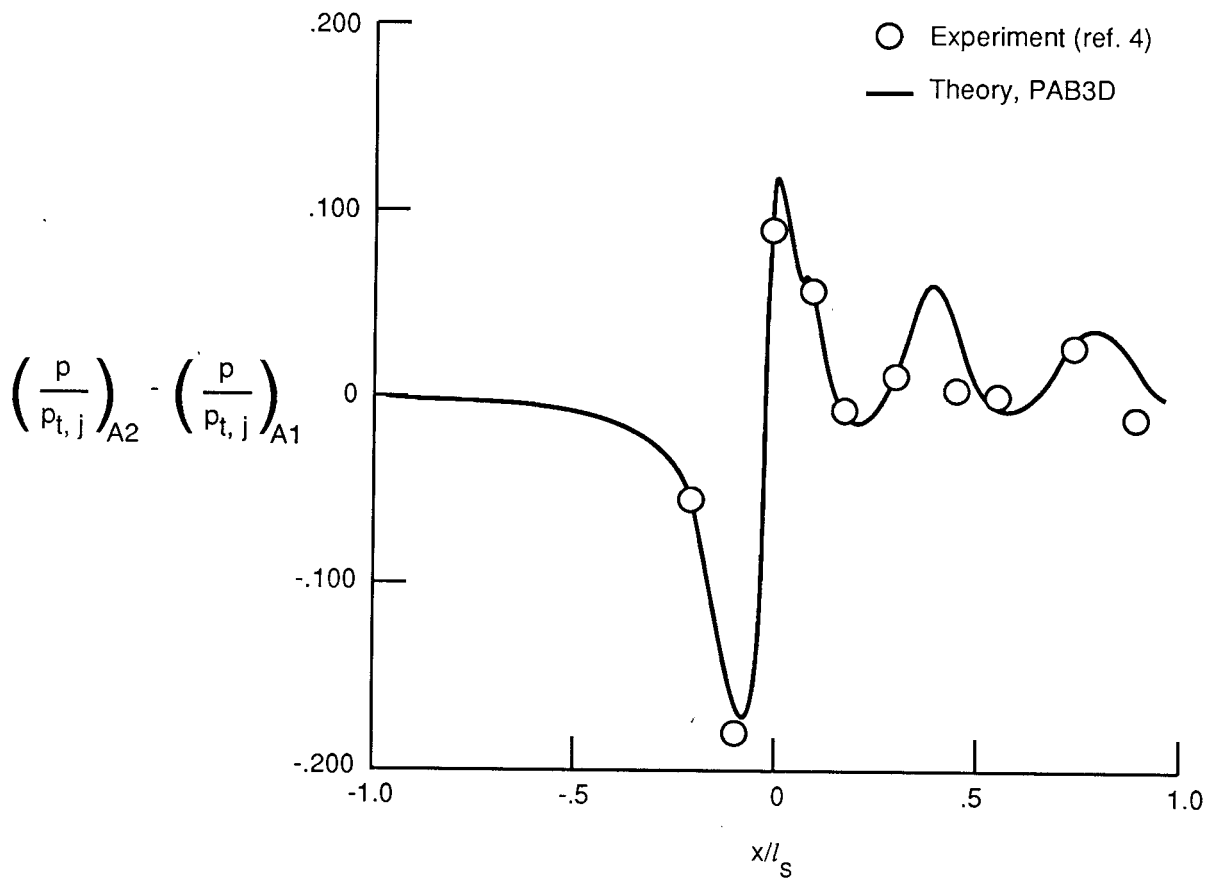


Figure 14. Experimental and theoretical increments in static pressure on upper-flap centerline due to change in nozzle throat radius for case 2. Dry power; design NPR.

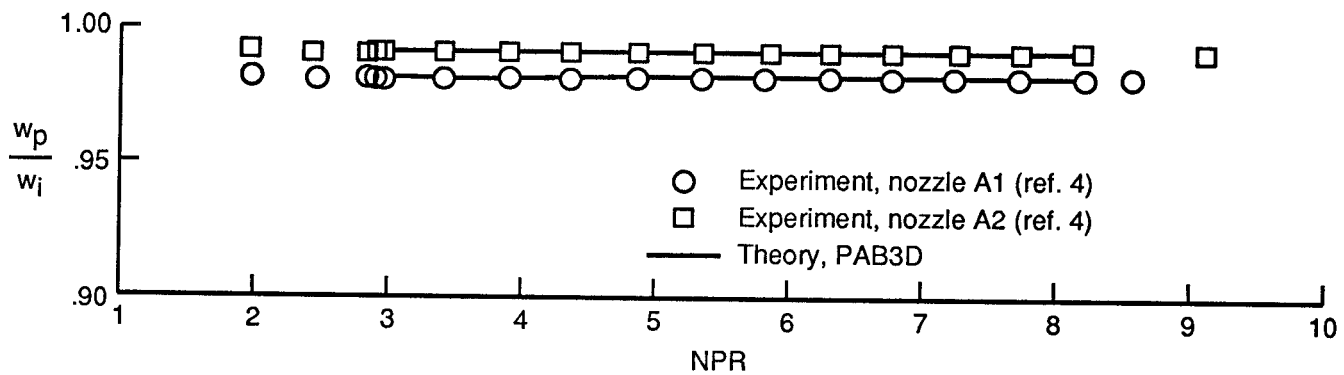
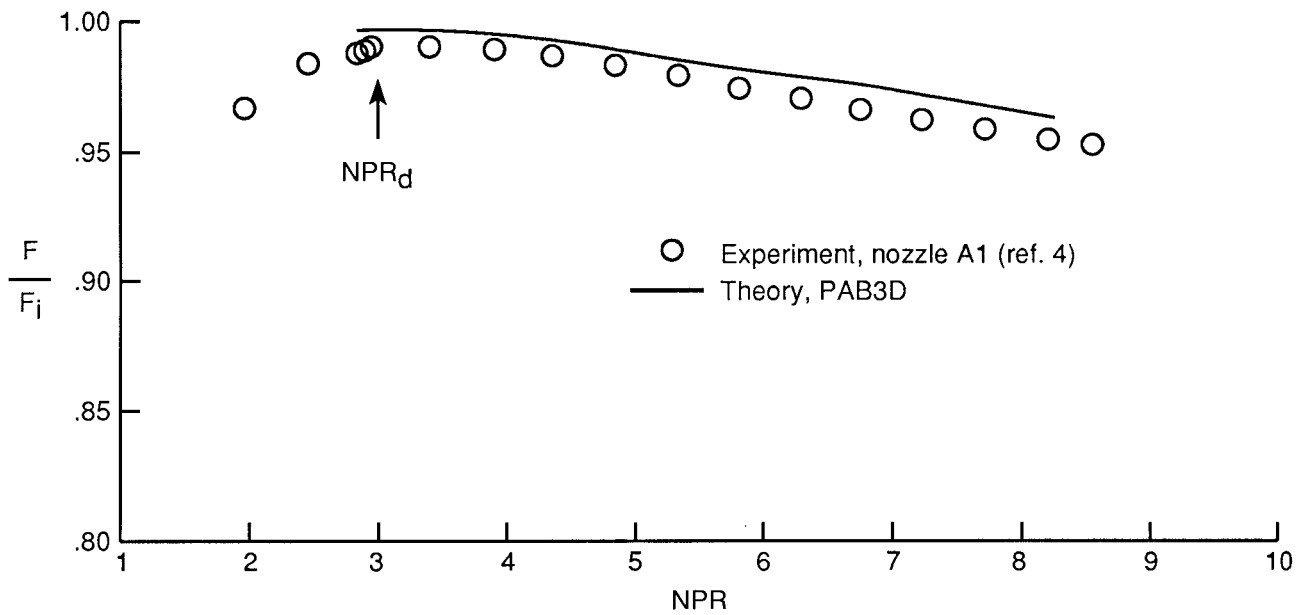
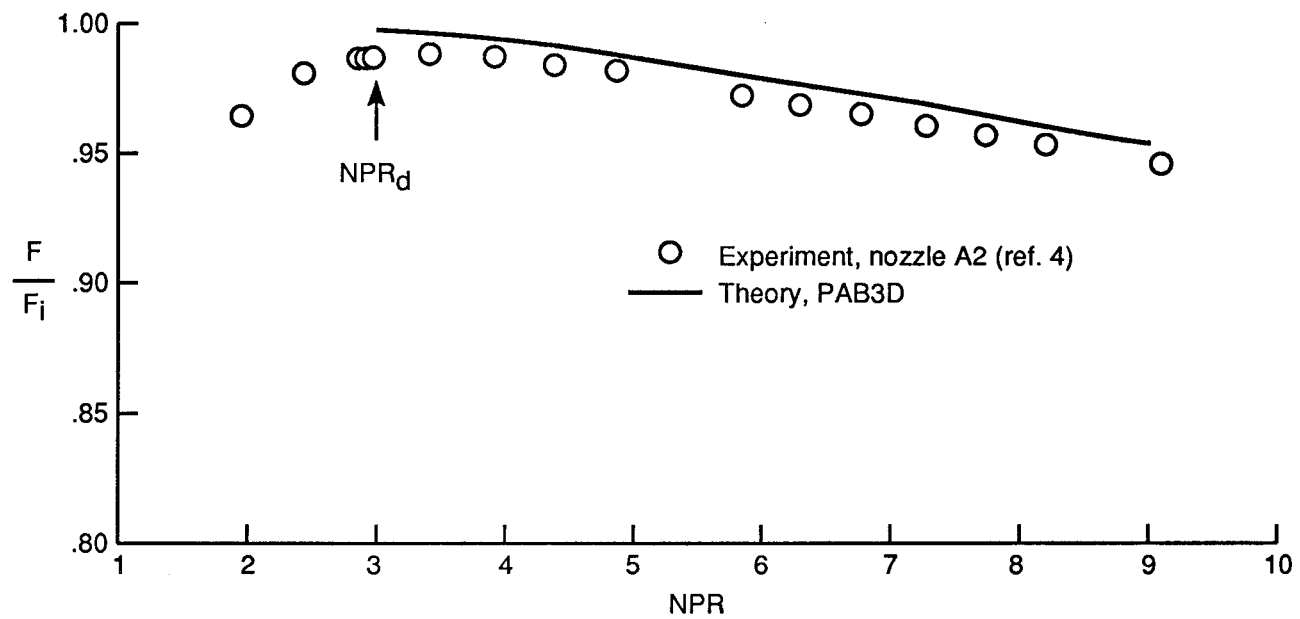


Figure 15. Predicted and experimentally determined discharge coefficients for case 2.



(a) Nozzle A1.



(b) Nozzle A2.

Figure 16. Experimental and theoretical internal thrust ratios for case 2.

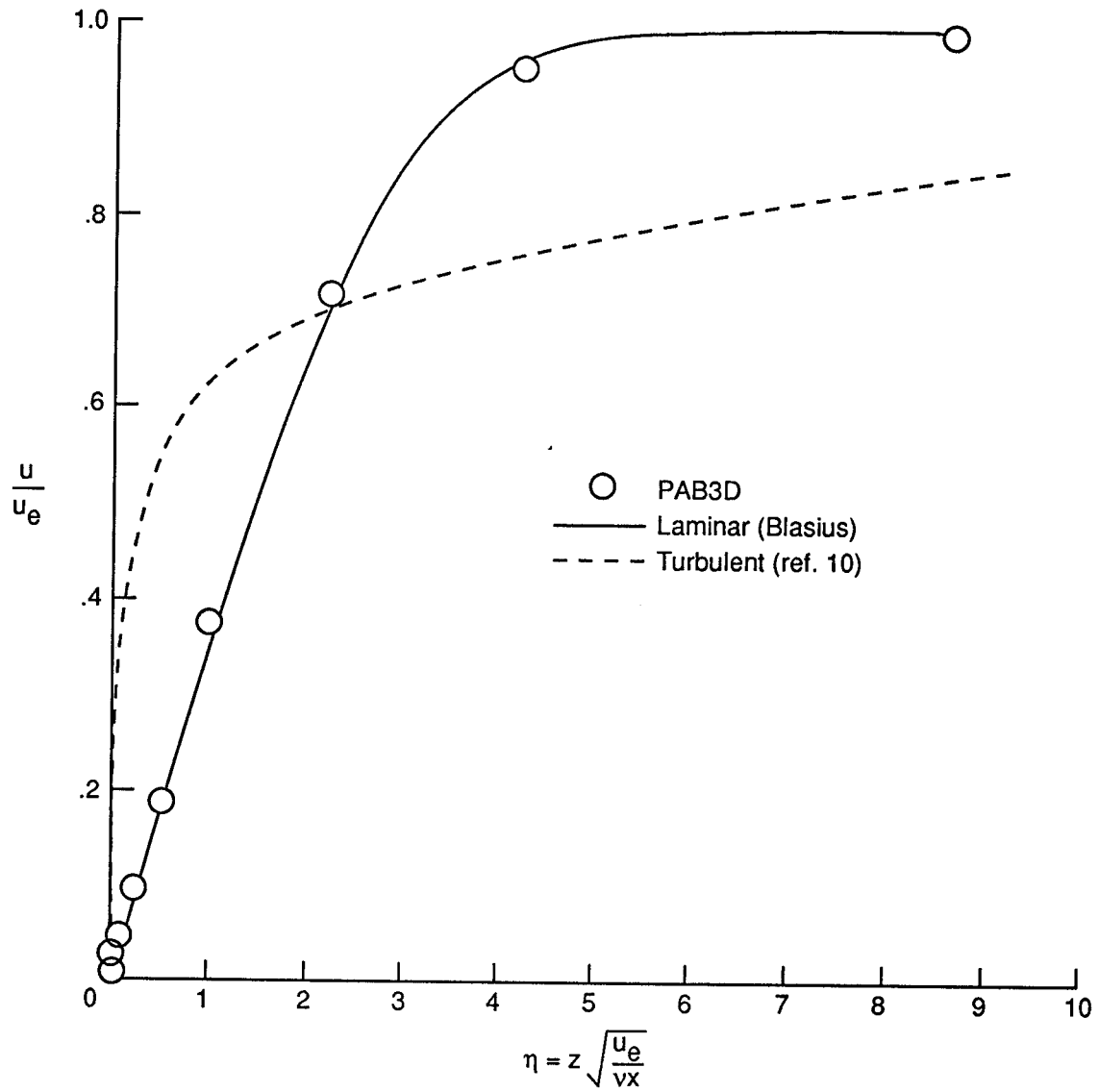


Figure 17. Calculated boundary-layer profile on divergent flap at nozzle exit for nozzle configuration A1.

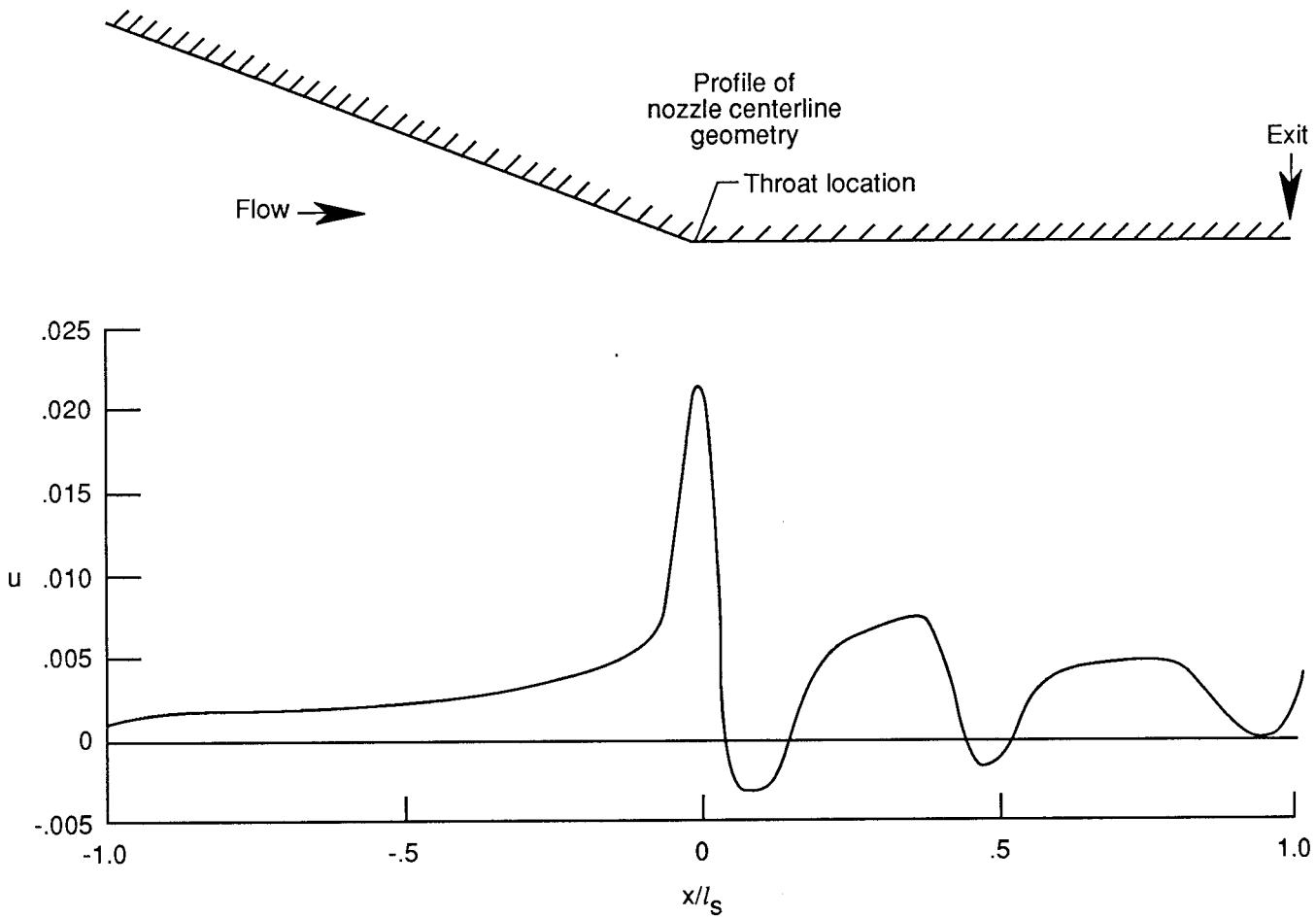


Figure 18. Distribution of streamwise component of velocity along centerline of divergent flap for nozzle A1.

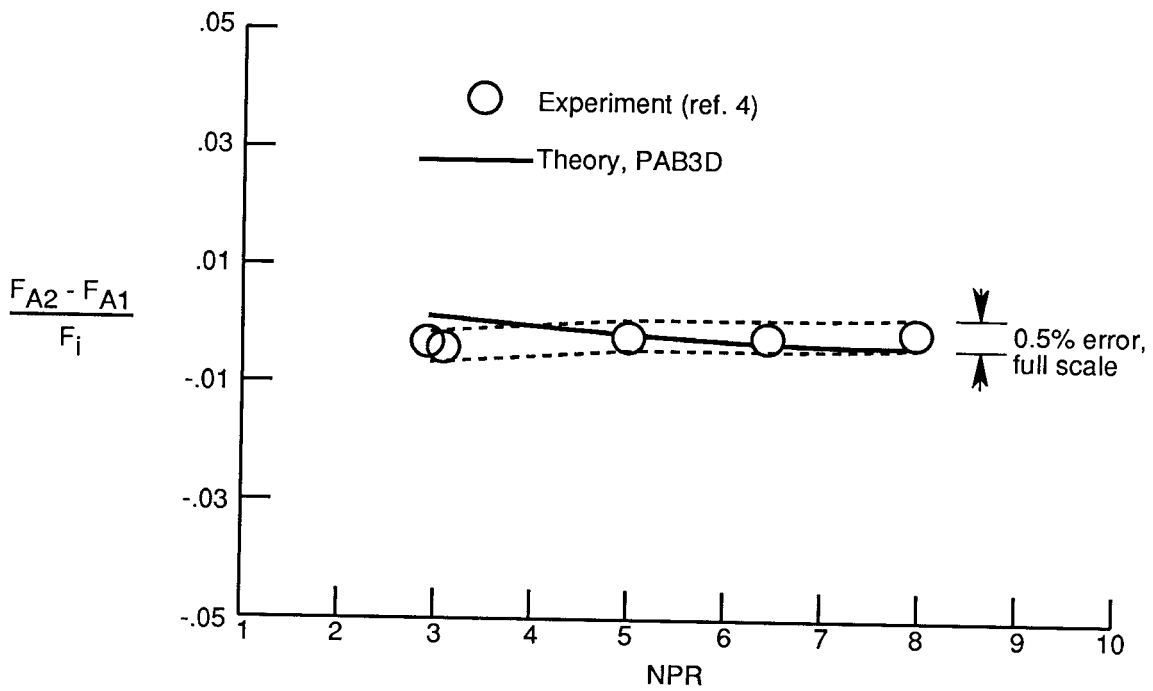
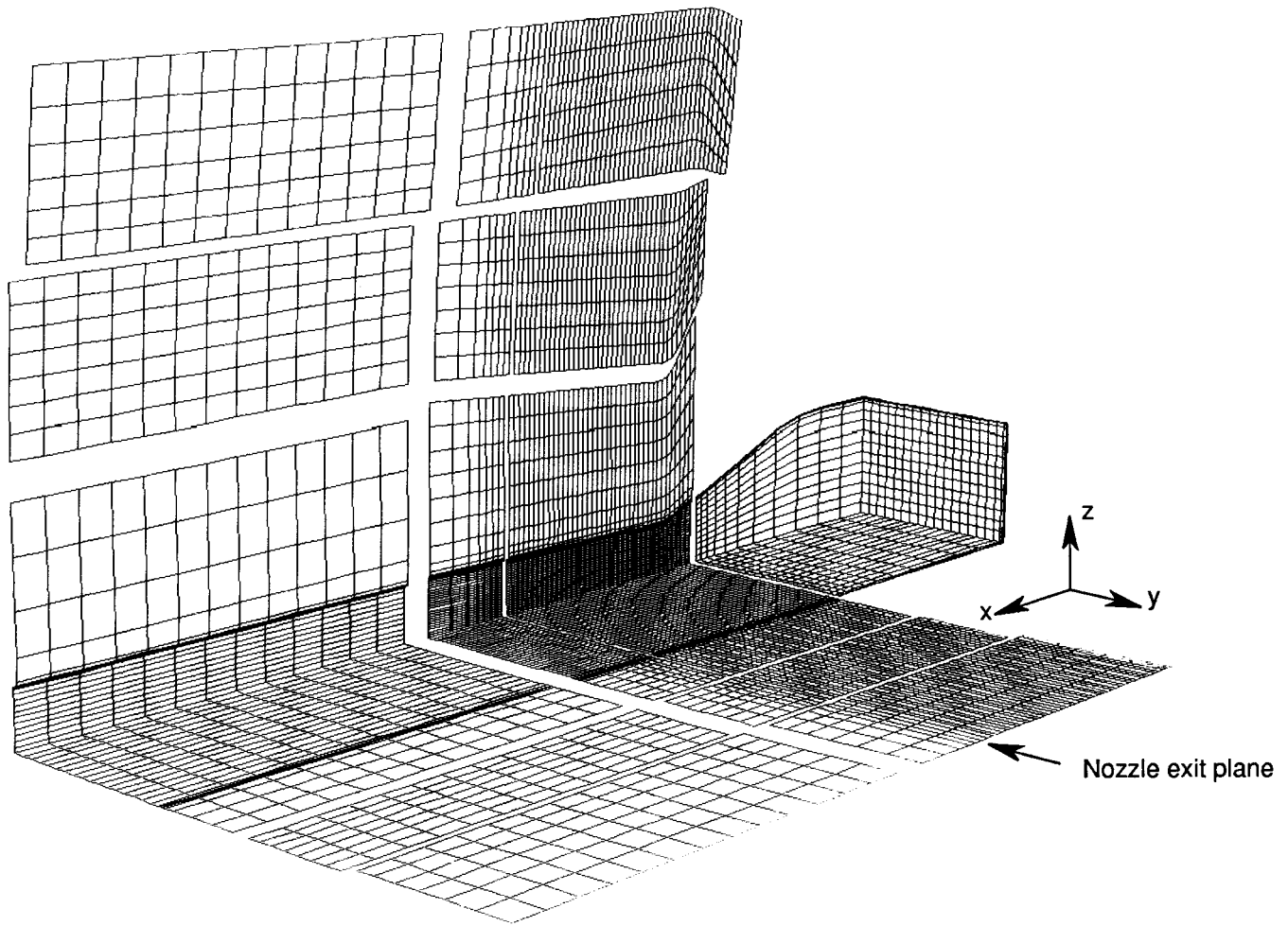
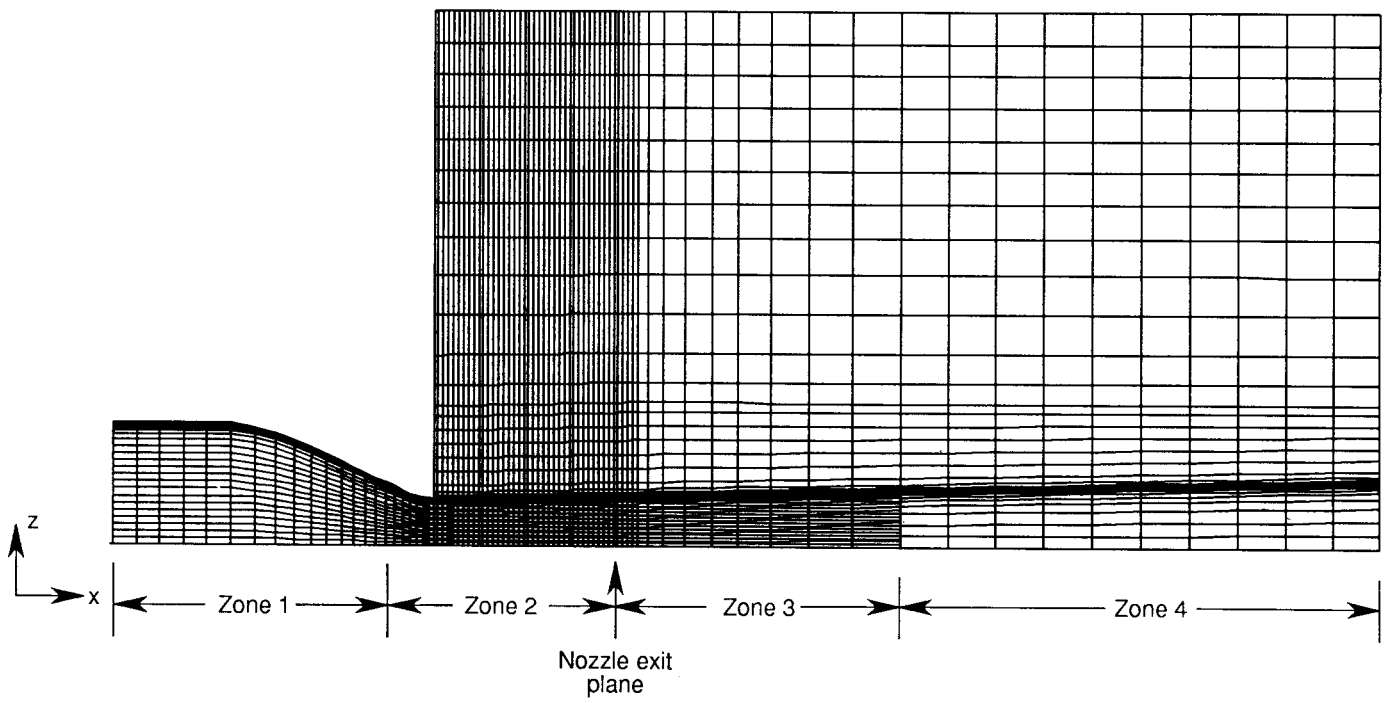


Figure 19. Experimental and theoretical increments in thrust ratio due to change in nozzle throat radius for case 2.



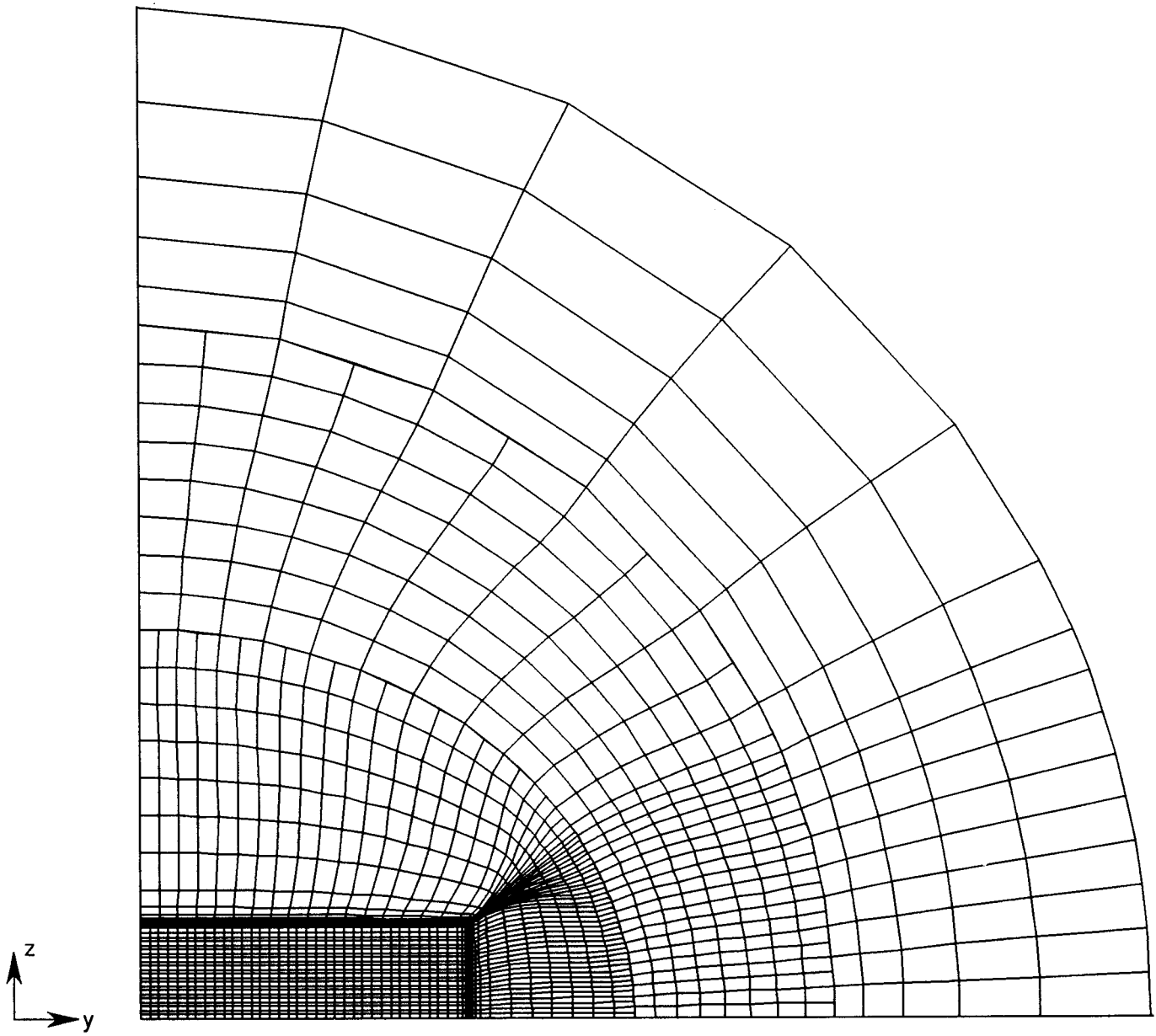
(a) Oblique view of cell-centered computational grid.

Figure 20. Grid for translating sidewall yaw vectoring study (case 3).



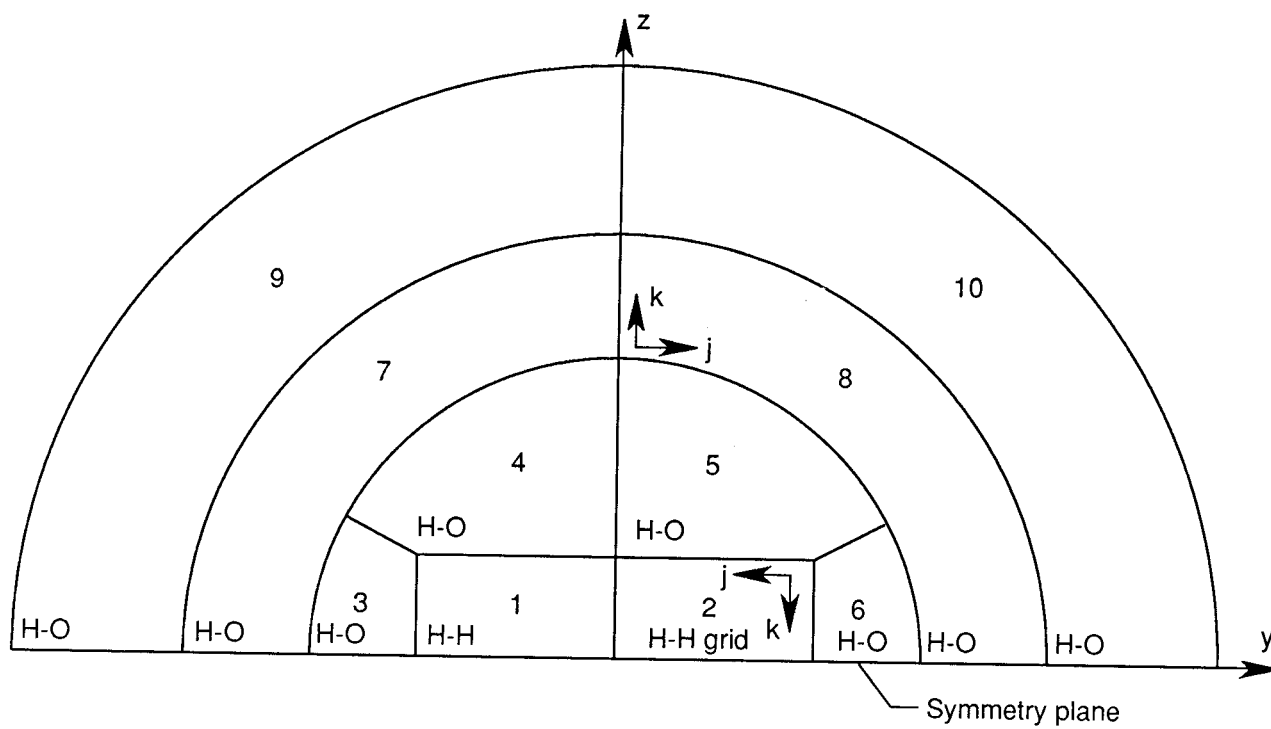
(b) Vertical sectional view of centerline plane of symmetry.

Figure 20. Continued.



(c) Vertical sectional view in plane of nozzle exit, one-quarter grid in lateral (ZY) plane.

Figure 20. Continued.



(d) Zone 2 blocking strategy of grid.

Figure 20. Concluded.

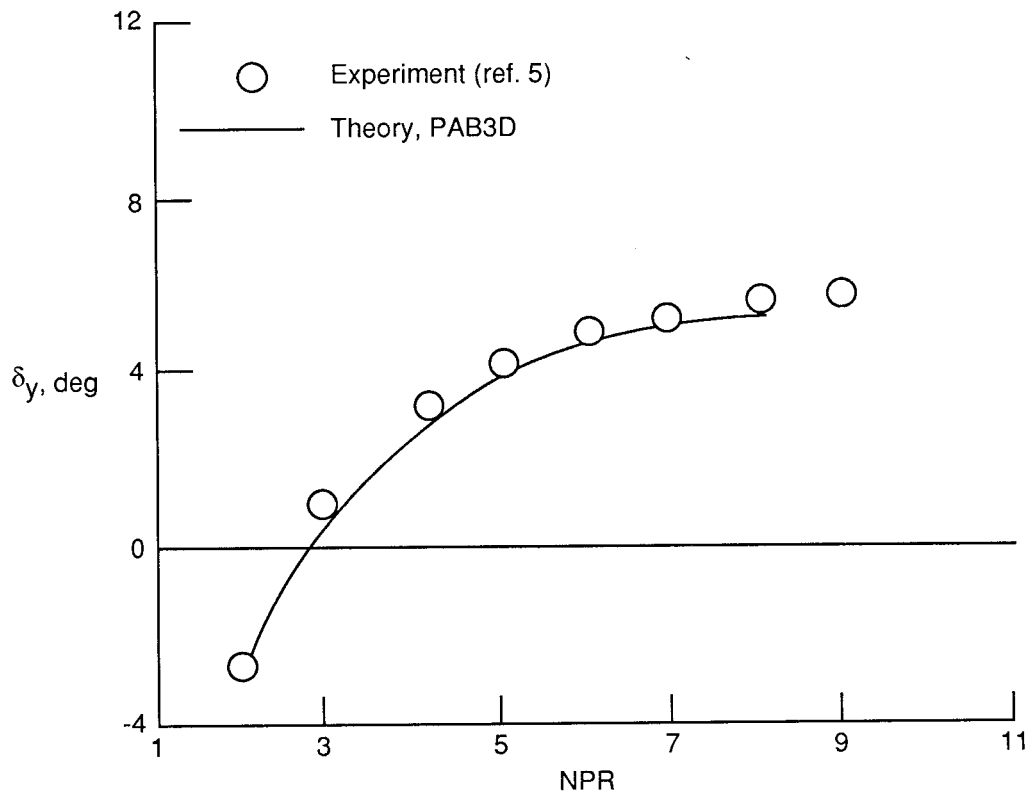


Figure 21. Predicted and experimentally determined changes in effective yaw vector angle with NPR for case 3. Dry power nozzle;  $(x_s - x_t)/l_s = 0.25$ .

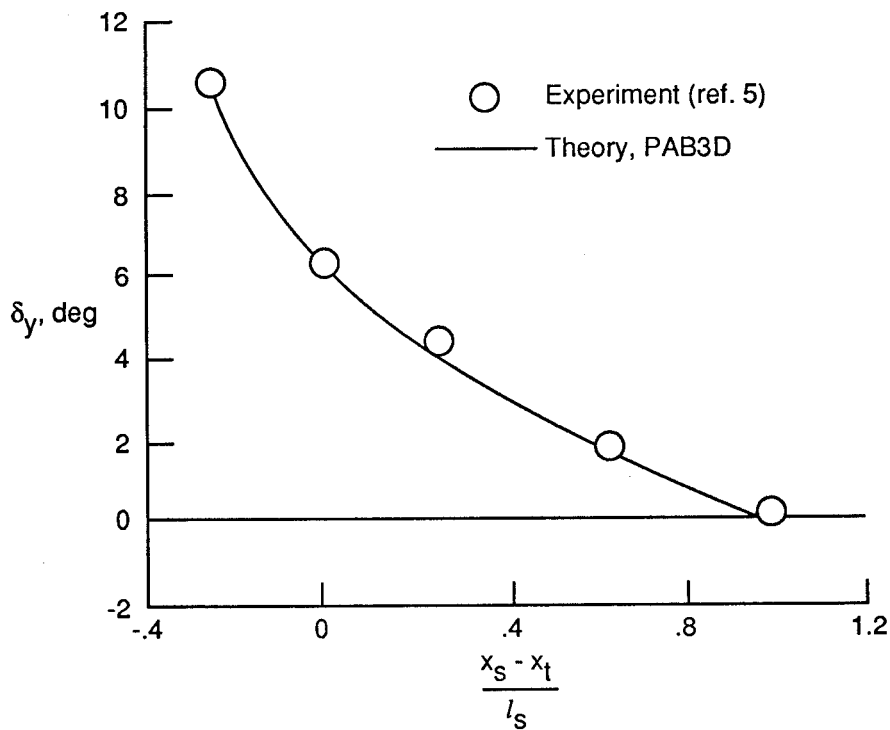
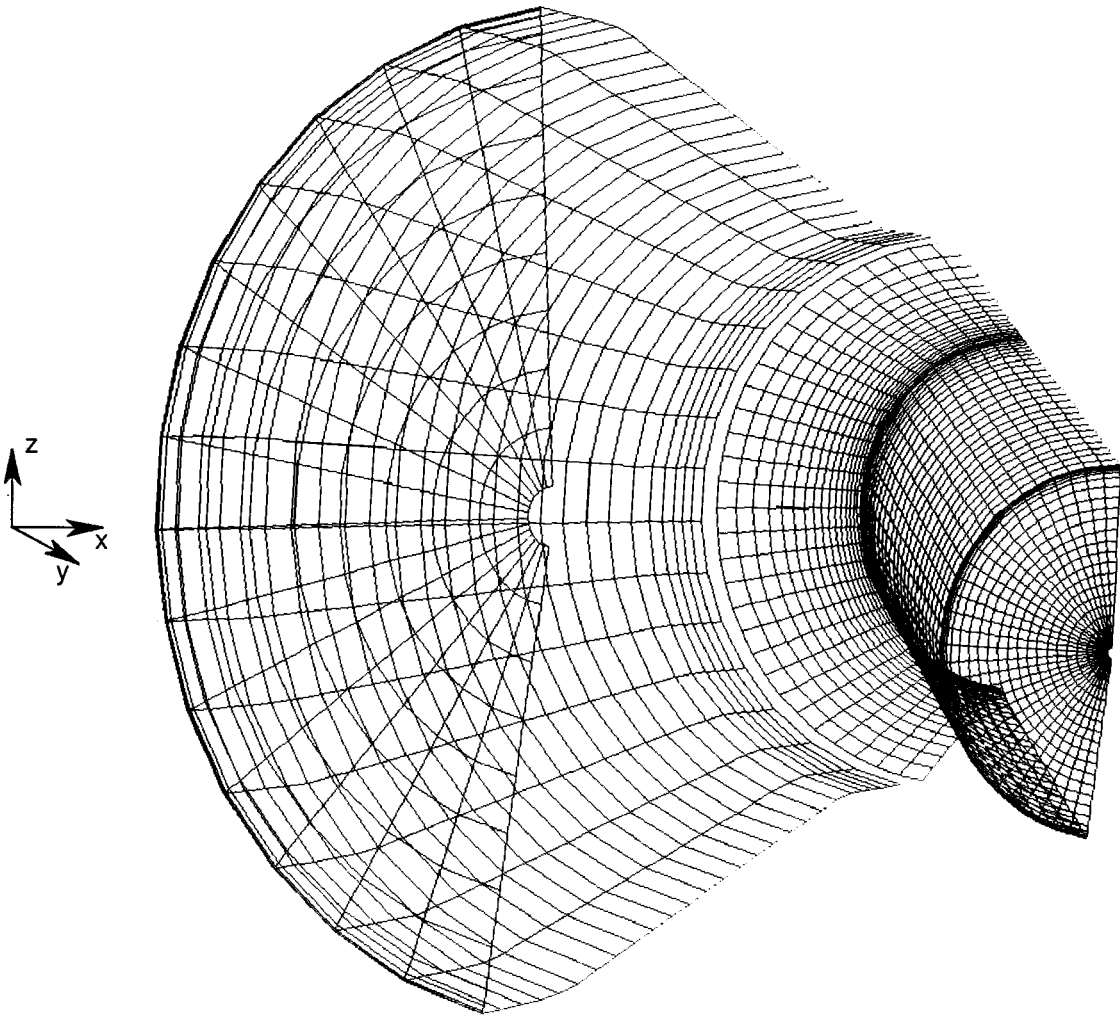
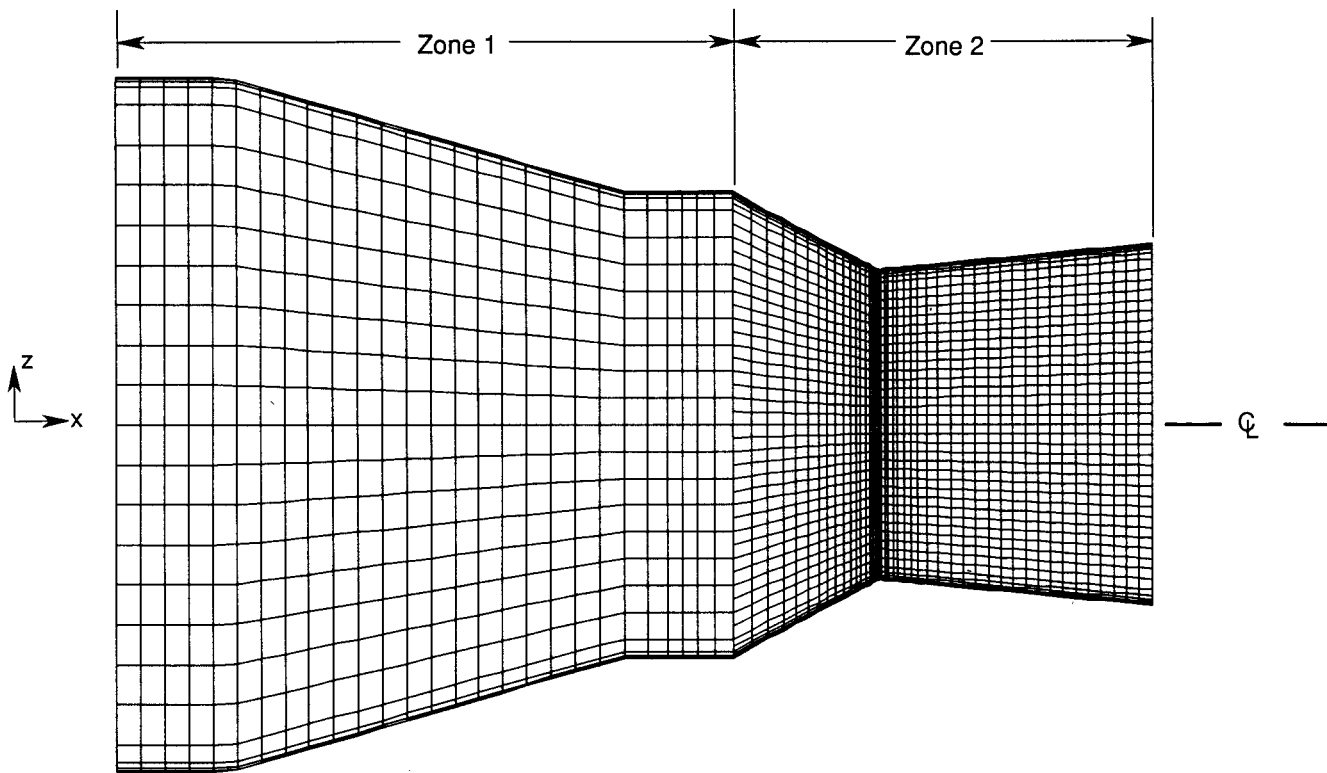


Figure 22. Predicted and experimentally determined changes in effective yaw vector angle with sidewall position for case 3. Dry power nozzle; NPR = 5.0.

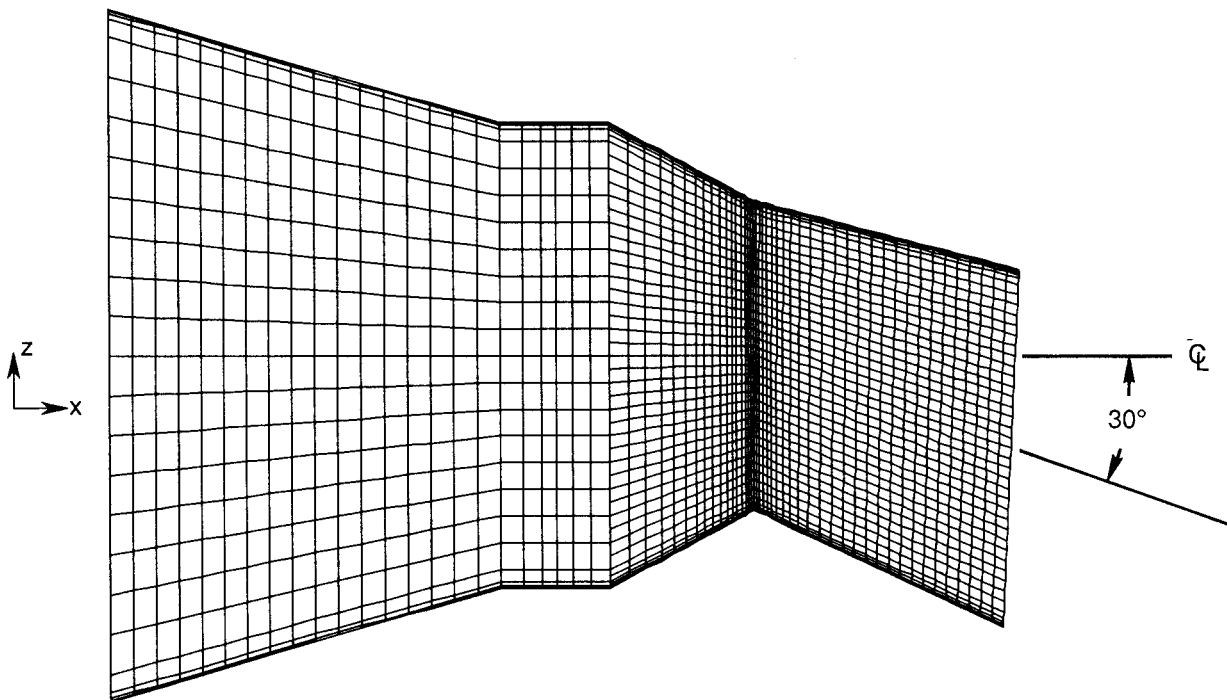


(a) Oblique view of cell-centered computational grid for nozzle vectored  $30^\circ$ .

Figure 23. Grid for multiaxis vectoring axisymmetric nozzle (case 4).

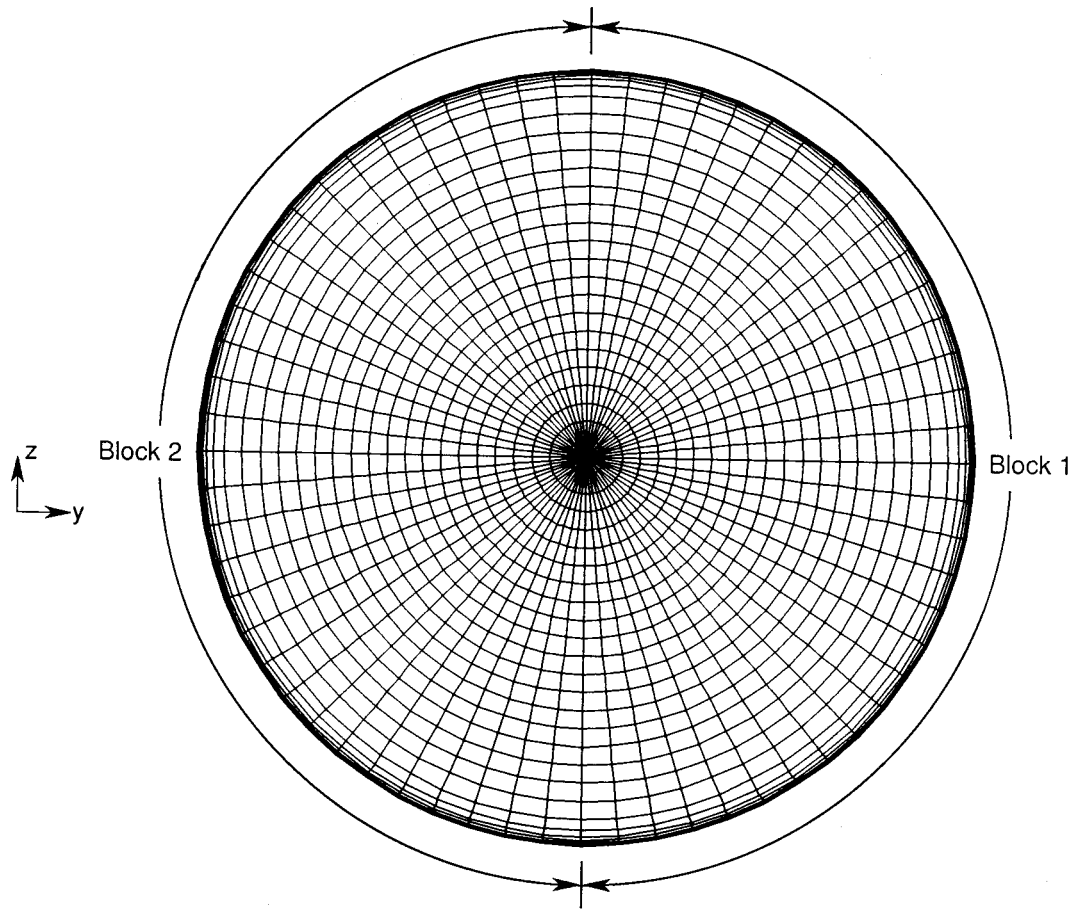


(b) Vertical centerline plane of symmetry of unvectored nozzle for short-flap, dry power geometry.



(c) Vertical centerline plane of symmetry of nozzle vectored  $30^\circ$  for short-flap, dry power geometry.

Figure 23. Continued.



(d) Cross-sectional view in plane of nozzle exit face.

Figure 23. Concluded.

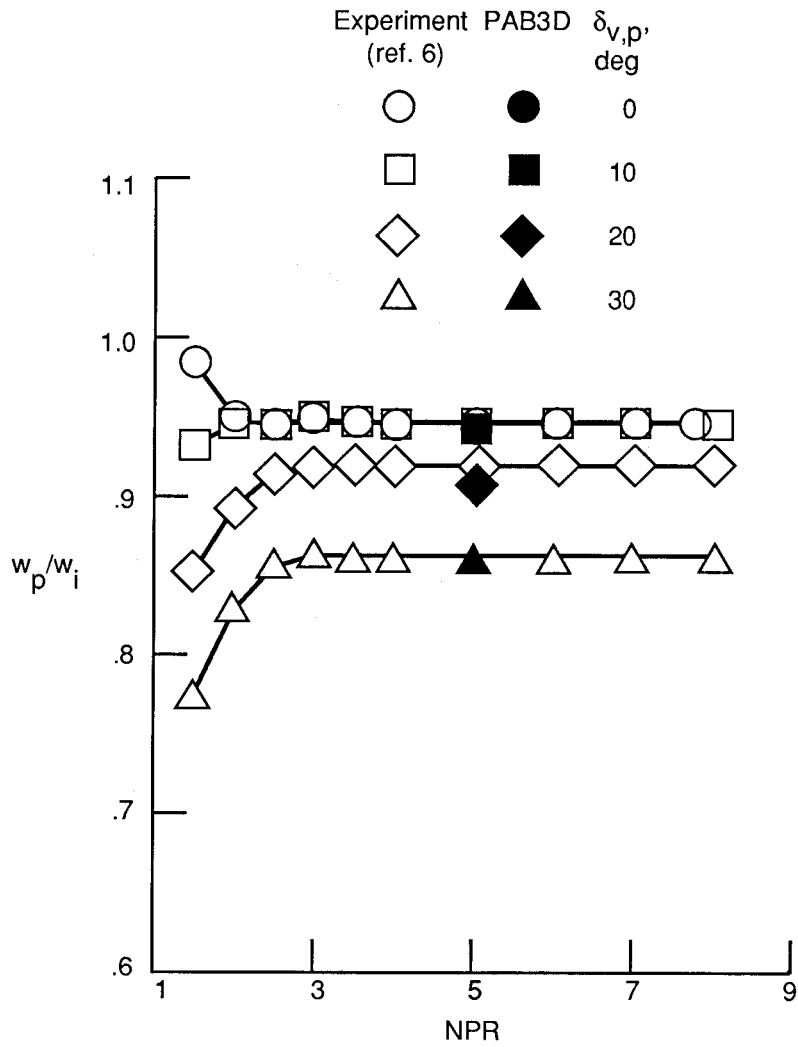


Figure 24. Predicted and experimentally determined discharge coefficients for case 4. Short-flap, dry power nozzle.

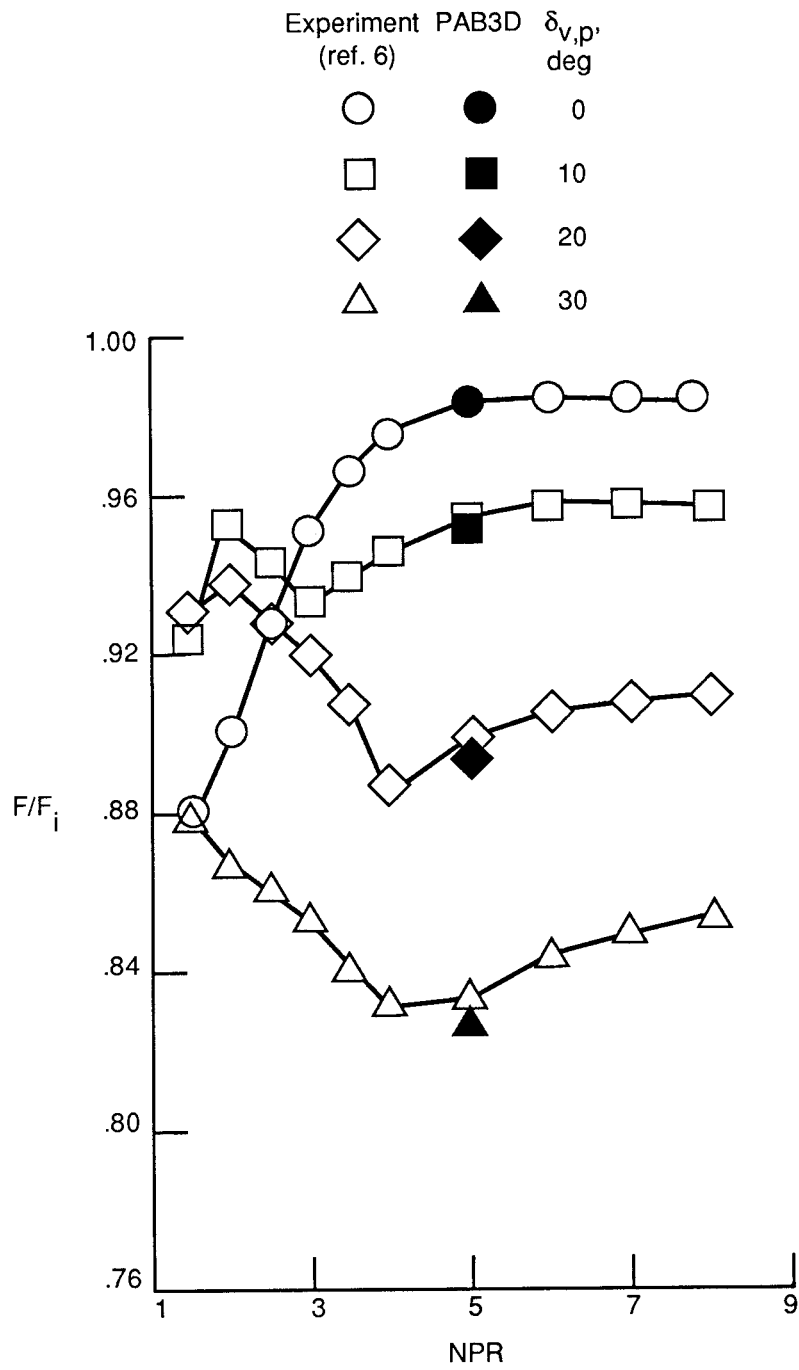


Figure 25. Predicted and experimentally determined thrust ratios for case 4. Short-flap, dry power nozzle.

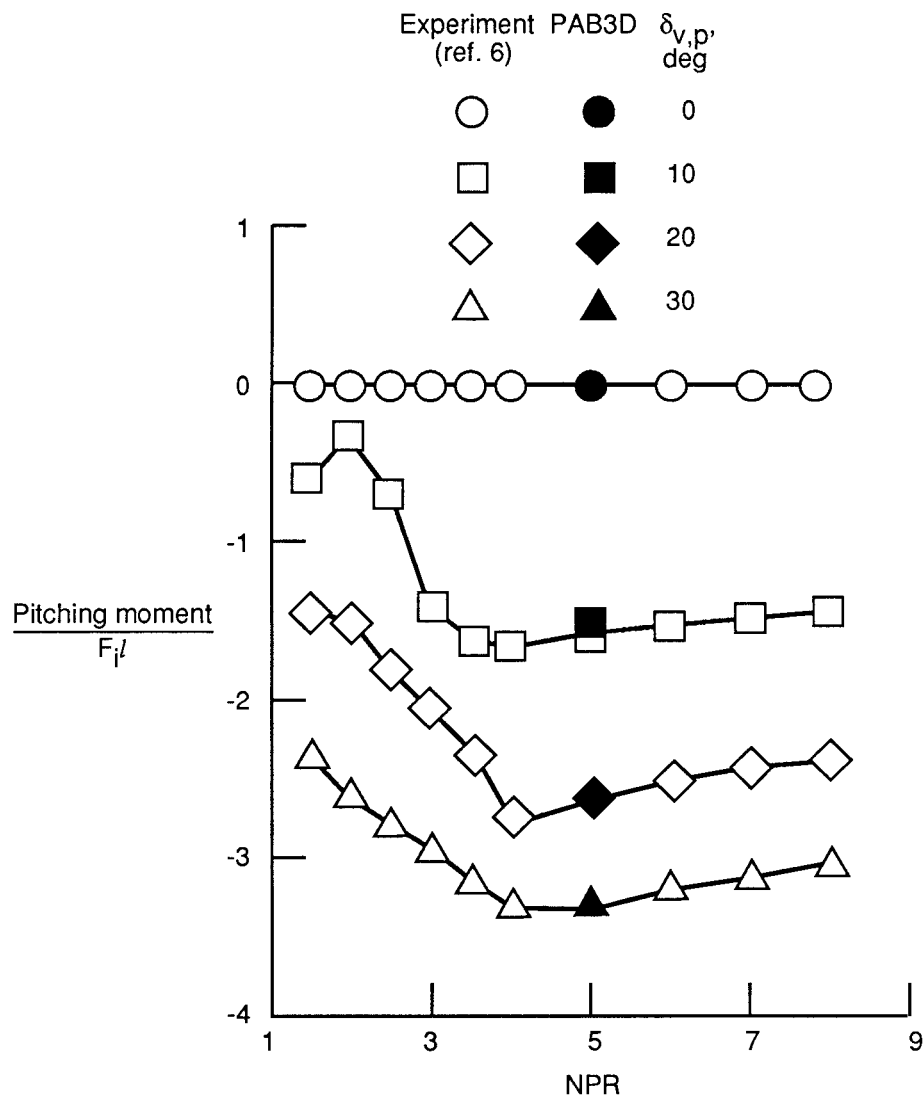
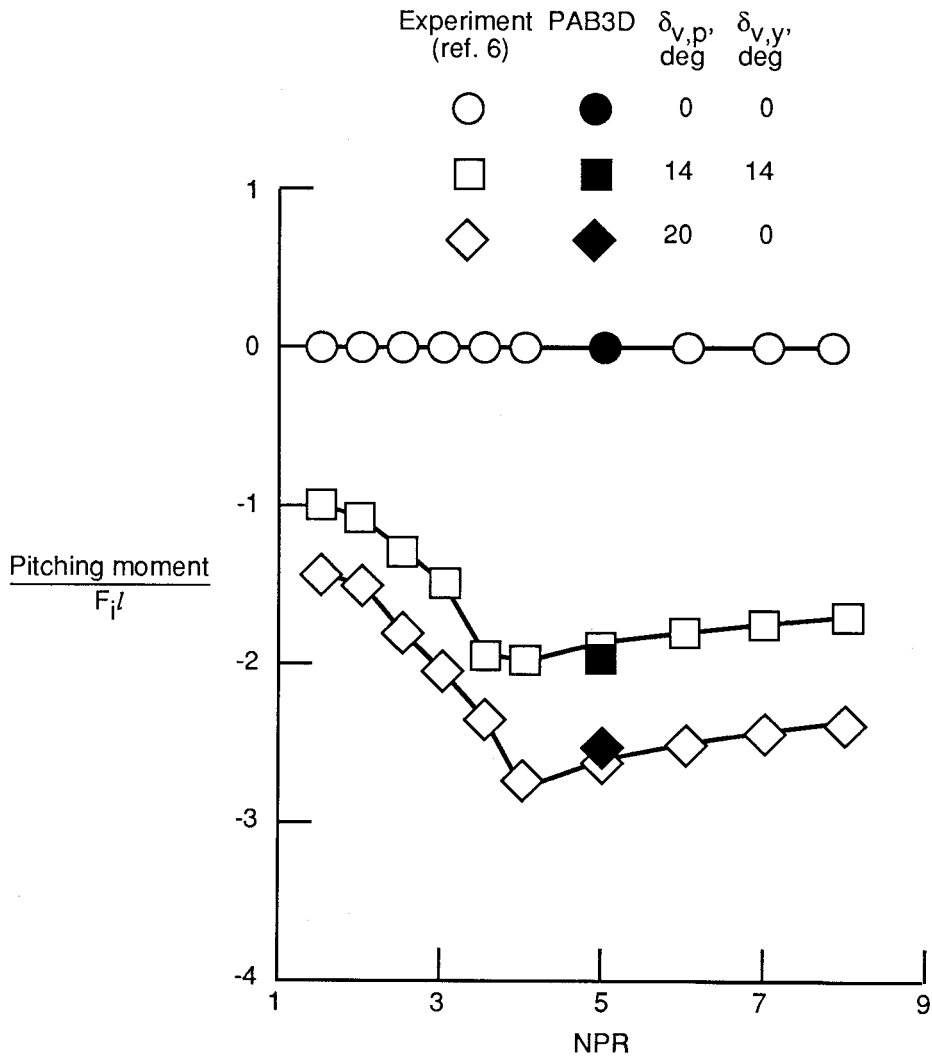
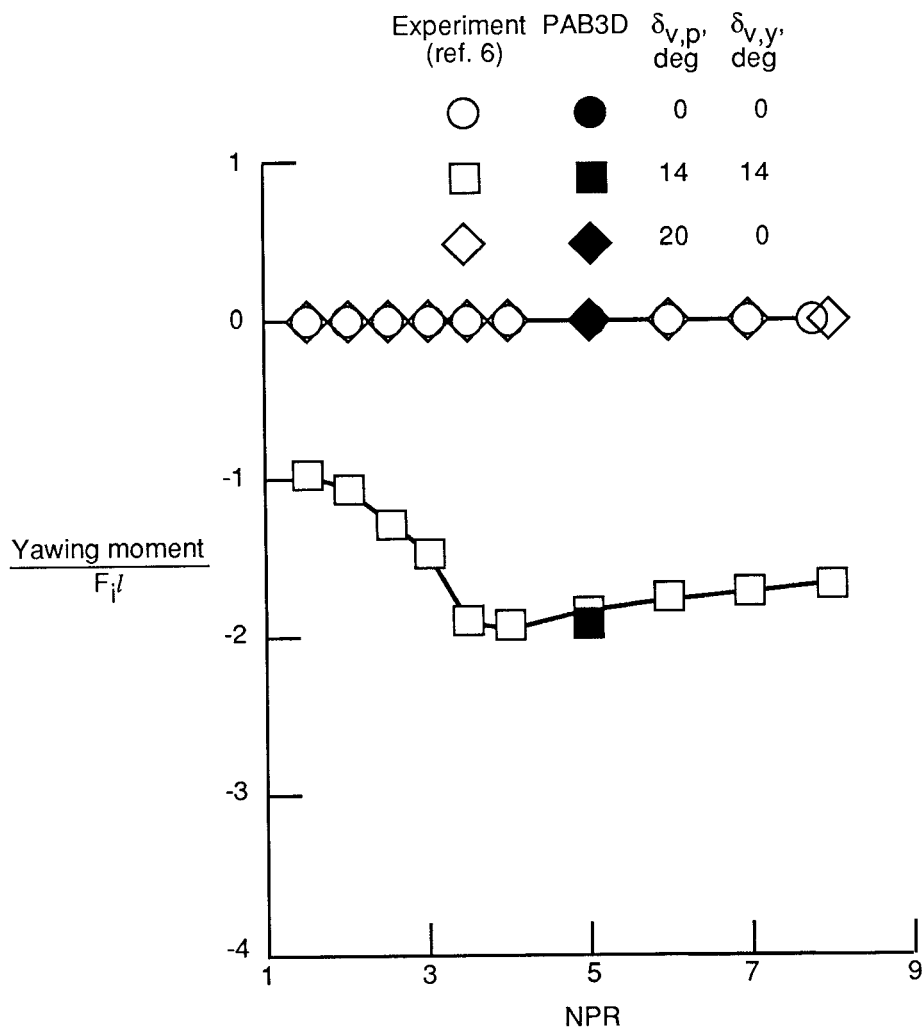


Figure 26. Predicted and experimentally determined pitching moments for case 4. Short-flap, dry power nozzle.



(a) Pitching moment.

Figure 27. Predicted and experimentally determined moments with multiaxis vectoring for case 4. Short-flap, dry power nozzle.



(b) Yawing moment.

Figure 27. Concluded.

REPORT DOCUMENTATION PAGE			Form Approved OMB No. 0704-0188	
Public reporting burden for this collection of information is estimated to average 1 hour per response, including the time for reviewing instructions, searching existing data sources, gathering and maintaining the data needed, and completing and reviewing the collection of information. Send comments regarding this burden estimate or any other aspect of this collection of information, including suggestions for reducing this burden, to Washington Headquarters Services, Directorate for Information Operations and Reports, 1215 Jefferson Davis Highway, Suite 1204, Arlington, VA 22202-4302, and to the Office of Management and Budget, Paperwork Reduction Project (0704-0188), Washington, DC 20503.				
1. AGENCY USE ONLY (Leave blank)	2. REPORT DATE October 1992	3. REPORT TYPE AND DATES COVERED Technical Paper		
4. TITLE AND SUBTITLE A Nozzle Internal Performance Prediction Method			5. FUNDING NUMBERS WU 505-62-30-01	
6. AUTHOR(S) John R. Carlson				
7. PERFORMING ORGANIZATION NAME(S) AND ADDRESS(ES) NASA Langley Research Center Hampton, VA 23681-0001			8. PERFORMING ORGANIZATION REPORT NUMBER L-16965	
9. SPONSORING/MONITORING AGENCY NAME(S) AND ADDRESS(ES) National Aeronautics and Space Administration Washington, DC 20546-0001			10. SPONSORING/MONITORING AGENCY REPORT NUMBER NASA TP-3221	
11. SUPPLEMENTARY NOTES				
12a. DISTRIBUTION/AVAILABILITY STATEMENT  Unclassified-Unlimited  Subject Category 02			12b. DISTRIBUTION CODE	
13. ABSTRACT (Maximum 200 words) A prediction method has been written and incorporated into a three-dimensional Navier-Stokes code (PAB3D) for the calculation of nozzle internal performance. The quantities calculated are discharge coefficient; normal, side, and axial thrust ratios; rolling, pitching, and yawing moments; and effective pitch and yaw vector angles. Four different case studies are presented to confirm the applicability of the methodology. Internal and, in most situations, external flow-field regions are required to be modeled. The computed nozzle discharge coefficient matches both the level and the trend of the experimental data within quoted experimental data accuracy (0.5 percent). Moment and force ratios are generally within 1 to 2 percent of the absolute level of experimental data, with the trends of data matched accurately.				
14. SUBJECT TERMS Nozzles; Nozzle performance; Computational fluid dynamics; Performance prediction			15. NUMBER OF PAGES 48	
			16. PRICE CODE A03	
17. SECURITY CLASSIFICATION OF REPORT Unclassified	18. SECURITY CLASSIFICATION OF THIS PAGE Unclassified	19. SECURITY CLASSIFICATION OF ABSTRACT	20. LIMITATION OF ABSTRACT	